

Dynamics of gaseous oxidized mercury at Villum Research Station during the High Arctic summer

Jakob Boyd Pernov, Bjarne Jensen, Andreas Massling, Daniel Charles Thomas, and Henrik Skov

Department of Environmental Science, iClimate, Arctic Research Center, Aarhus University, Frederiksborgvej 399, 4000
5 Roskilde, Denmark

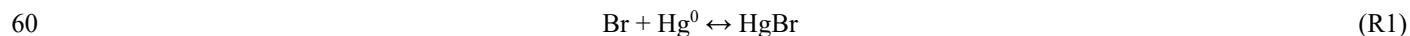
Correspondence: Jakob Boyd Pernov (jbp@envs.au.dk)

Abstract. While much research has been devoted to the subject of gaseous elemental mercury (GEM) and gaseous oxidized mercury (GOM) in the Arctic spring, during atmospheric mercury depletion events, few studies have examined the behavior of GOM in the High Arctic summer. GOM, once deposited and incorporated into the ecosystem, can pose a threat to human
10 and wildlife health, though there remain large uncertainties regarding the transformation, deposition, and assimilation of mercury into the food web. Therefore, to further our understanding of the dynamics of GOM in the High Arctic during the late summer, we performed measurements of GEM and GOM along with meteorological parameters, atmospheric constituents, and utilized modeled air mass history during two summer campaigns in 2019 and 2020 at Villum Research Station (Villum) in Northeastern Greenland. Seven events of enhanced GOM concentrations were identified and investigated in greater detail.
15 In general, the common factors associated with event periods at ground level were higher levels of radiation, lower H₂O mixing ratios, accumulated precipitation, and RH, although none were connected with cold temperatures. Non-event periods at ground level each displayed a different pattern, in one or more parameters, when compared to event periods. Generally, air masses during event periods for both campaigns were colder, drier, arrived from higher altitudes, spent more time above the mixed layer, and less time in a cloud compared to non-events, although some events deviated from this general pattern. Non-event
20 air masses displayed a different pattern in one or more parameters when compared to event periods although were generally warmer, wetter, arrived from lower altitudes with little radiation. Coarse mode aerosols were hypothesized to provide the heterogeneous surface for halogen propagation during some of the events while for others the source is unknown. While these general patterns were observed for event and non-event periods, analysis of individual events showed more specific origins. Five of the seven events were associated with air masses that experienced similar conditions: transported from the cold, dry,
25 sunlit free troposphere. However, two events experienced contrasting conditions, with air masses being warm and wet with surface layer contact under little radiation. Two episodes of extremely high levels of N_{Coarse} and BC, which appear to originate from flaring emissions in Russia, did not contribute to enhanced GOM levels. This work aims to provide a better understanding of the dynamics of GOM during the High Arctic summer.

1 Introduction

30 Gaseous elemental mercury (Hg^0 or GEM) is a ubiquitous pollutant in the atmosphere due to its long relaxation time (6 to 12 months; relaxation time refers to the time delay between emission reductions and effect on ambient concentrations), thus being subject to long-range transport from source regions to remote environments through deposition and reemission cycling (Pirrone et al., 2010; Skov et al., 2020). The sources of mercury include anthropogenic emissions, e.g., fossil fuel/biomass combustion, and artisanal small-scale gold mines, in addition to natural emissions such as volcanoes, biomass burning, ocean/soil evasion, and reemission of previously deposited/legacy mercury (AMAP, 2011). In the atmosphere, GEM is oxidized to its divalent form (Hg^{II}), commonly known as gaseous oxidized mercury (GOM). GOM has a much shorter residence time than GEM in the atmosphere owing to its higher solubility, lower vapor pressure, and faster deposition velocity (Skov et al., 2006). Mercury can also be present in aerosol particles, referred to as particulate bound mercury (PHg), either through GOM condensation or through heterogeneous reactions of GEM on aerosol surfaces (Durnford and Dastoor, 2011). In the polar regions, GEM typically dominates the atmospheric distribution throughout the year, with smaller contributions from GOM and PHg. However, during depletion events in the spring, GOM and PHg can constitute large fractions of total atmospheric mercury (Steffen et al., 2014). In contrast to the polar regions, the mid-latitudes, and especially locations close to anthropogenic emission point sources, GOM and PHg can be emitted directly to the atmosphere and represent significant fractions of the atmospheric mercury burden (Muntean et al., 2018).

45 In locations with elevated reactive halogen concentrations (e.g., polar environments, the marine boundary layer, volcanic plumes, and salt lakes) and especially bromine radicals, GEM is quickly transformed into GOM (Obrist et al., 2010; von Glasow, 2010; Angot et al., 2016; Ye et al., 2016; Wang et al., 2019). In the Arctic, this process manifests as atmospheric mercury depletion events (AMDEs), which occur in spring following polar sunrise, and result in the rapid depletion (on the order of hours) of GEM and conversion to GOM (Schroeder et al., 1998; Lindberg et al., 2002; Berg et al., 2003; Skov et al., 2004). In the early spring at Alert, Nunavut, Canada, it has been demonstrated that GOM is converted to PHg (through condensational processes due to the cold temperatures and high aerosol surface area concentration (Freud et al., 2017)) while in the late spring oxidized mercury is mainly present as GOM (due to reduced surface area and increased temperatures) (Steffen et al., 2014). Late spring is also the peak of total Hg in surface snow at Alert, Nunavut, Canada and Utqiagvik, Alaska, USA (formerly Barrow), indicating that dry deposition of GOM is a major pathway of mercury into the ecosystem (Lu et al., 2001; Lindberg et al., 2002; Steffen et al., 2002; Steffen et al., 2014). GEM oxidation has been demonstrated to be initiated via photochemical reactions with the Br radical (R1-R2) through modeling studies (Holmes et al., 2006; Holmes et al., 2010; Horowitz et al., 2017), kinetic studies (Donohoue et al., 2006), theoretical studies (Goodsite et al., 2004; Dibble et al., 2012; Goodsite et al., 2012), and observations (Skov et al., 2004; Stephens et al., 2012; Wang et al., 2019).



Where Y could be OH, O₃, NO₂, HO₂, Br, Cl, BrO, ClO, I, IO (Holmes et al., 2006; Hynes et al., 2009; Holmes et al., 2010; Dibble et al., 2012; Jiao and Dibble, 2017b, a). Of which Br, I, and OH have been postulated to be the main species for Y, both globally and in the Arctic (Goodsite et al., 2004, 2012), while NO₂, HO₂, ClO, or BrO have been demonstrated to be candidates for Y by Dibble et al. (2012). Recently, ozone was proposed to be a missing oxidation pathway of HgBr (Saiz-Lopez et al., 2020). Sources of these reactive halogen species include emissions from sea ice, snowpack, frost flowers, refreezing leads, sea-salt aerosol, and labile halogen reservoir species (i.e., halocarbons and inorganic bromine) (Brooks et al., 2006; Kaleschke et al., 2004; Peterson et al., 2018, 2019; Simpson et al., 2015). The exact chemical formulas for GOM and PHg are currently unknown so both species are operationally defined by their detection methods (Landis et al., 2002; Angot et al., 2016), although the development of improved analytical systems for their detection is currently underway (Gustin et al., 2021). Once formed, GOM can either bind to aerosol particles, becoming PHg, or deposit onto the snowpack through dry and wet deposition. The majority of this deposited mercury is photo-reduced and emitted back into the atmosphere (Brooks et al., 2006; Dastoor et al., 2008; Kamp et al., 2018). The snowpack will retain a fraction of this mercury and release it with the ionic pulse during the melt season, introducing mercury into the ecosystem (Lu et al., 2001; Ariya et al., 2004; Durnford and Dastoor, 2011; Douglas et al., 2017). Recently, isotope analysis has revealed GEM uptake by vegetation and soils to be the main source of mercury input to the terrestrial environment in Alaska (Douglas and Blum, 2019; Jiskra et al., 2019), although this process has yet to be confirmed in the High Arctic.

After deposition, GOM can be methylated through biotic and abiotic processes to organic mercury (methyl- and dimethylmercury) (Macdonald and Loseto, 2010; Møller et al., 2011). Organic mercury is an extremely powerful neurotoxin that bio-accumulates in upper trophic levels thus posing a threat to ecosystems and human health (especially in indigenous peoples in high latitudes and societies that rely heavily on a seafood diet) (Park and Zheng, 2012). Therefore, as the Arctic becomes more populated and continues to change it is important to understand mercury oxidation in response to a changing climate, especially in high latitude regions (AMAP, 2011; Durnford and Dastoor, 2011; Stern et al., 2012).

While the majority of GOM formation and deposition occurs in the Arctic during spring, little attention has been given to the behavior of GOM outside of AMDEs. Steen et al. (2011) reported high amounts of GOM (max > 120 pg m⁻³, mean 8 ± 13 pg m⁻³) during the summers of 2007 and 2008 at Zeppelin Mountain (79.93° N 11.50° E, 474 m above sea level). This study revealed a pattern of GOM previously unknown to the Arctic, with elevated GOM concentrations during the summer, which postulates GOM deposition occurs outside of AMDEs in the Arctic. They concluded the presence of GOM was of regional origin, as long-range transport of direct emissions from anthropogenic sources was unlikely. Other studies have found contrasting results regarding Arctic GOM concentrations during summer. During a research expedition in the Arctic Ocean in June–August 2004, Aspino et al. (2006) measured GEM, GOM, and PHg, and found increases in GEM over areas with > 70 % sea ice concentrations, which were attributed to an enhanced reduction potential and increased evasion of supersaturated dissolved mercury from the ocean through open leads. However, they found lower levels of GOM (< 20 pg m⁻³) and PHg (< 10 pg m⁻³) compared to Steen et al. (2011). Levels of Hg in snow and melt ponds were low (< 10 ng L⁻¹)

suggesting marginal accumulation of deposited mercury throughout the summer. Concentrations of GEM, GOM, PHg, CO, and ozone were also reported on a research cruise throughout the Arctic basin from July–September 2005 (Sommar et al., 2010). They found low levels of GOM ($3.2 \pm 1.7 \text{ pg m}^{-3}$) and PHg ($1.0 \pm 0.7 \text{ pg m}^{-3}$), which were not correlated with GEM, sunlight, nor ozone. Steffen et al. (2014) analyzed GOM and PHg at Alert, Nunavut, Canada from 2002–2011, they reported median values during July–September of 5.3–7.36 pg m^{-3} and 1.01–14.78 pg m^{-3} for PHg and GOM, respectively. The source of GOM during this study was unclear. While these latter studies found relatively low levels of GOM, the presence of GOM at all indicates that mercury oxidation and deposition are occurring outside of AMDEs in the Arctic.

With only limited measurements of GOM performed in the High Arctic summertime, there are many questions still unanswered. The dynamics of GOM in the Arctic are extremely complex; uncertainties in its spatiotemporal variability, annual cycle, and formation mechanisms emphasize the need for further examination. The Arctic region is undergoing rapid changes due to anthropogenic climate change and the dynamics of mercury oxidation are poorly resolved, especially in summer. Understanding these dynamics can offer insight into the general chemistry during Arctic summer and atmospheric mercury will respond to future changes in the Arctic climate. It is also important to understand the changes in mercury concentrations in the Arctic to assess the effects of abatement strategies of the Minamata Convention (UNEP, 2013) globally. This will aid in understanding what will be the effects of decreasing anthropogenic mercury emissions and global climate change on the recycling of mercury between different environmental matrixes and how it is ultimately sequestered.

Here we report measurements of GEM and GOM, outside of AMDEs, during the late summer of 2019 and GEM and GOM as well as PHg in the late summer of 2020 at Villum Research Station (Villum). We investigate the levels of GOM in connection with meteorological parameters, ozone, aerosol particle physical properties, and air mass history and examine existing interconnections and dependencies. In the following section, we describe the measurement site, analytical instrumentation, and analysis methods. We will then examine the results of the two campaigns in relation to meteorological parameters and atmospheric constituents as well as air mass history. We then discuss the factors influencing event vs. non-event periods as well as individual events. We conclude with a summary and consider the implications for mercury oxidation in a future climate.

120 **2 Methods and instrumentation**

2.1 Measurement sites

Measurements were performed at Flyger’s hut (N 81° 36’, W 16° 40’), which is part of Villum (81.6° N 16.67° W, 24 m above sea level) located on the Danish military base Station Nord in Northeastern Greenland. Villum and Flyger’s hut are both located approx. 2 kilometers to the south of Station Nord, they are separated by approx. 200 meters’ distance and they are both upwind > 95% of the time from local pollution sources at the military base. All times are reported as UTC.

2.2 Atmospheric mercury measurements

In 2019, atmospheric measurements of GEM and GOM at Flyger's hut started on August 16 and ended on September 1. In 2020, measurements of GEM, GOM, and PHg started on July 17 and ended on August 4. GEM was analyzed on a 5-minute time resolution by a Tekran 2537A vapor phase analyzer at a flow rate of 1 L min⁻¹. This technique is based on the pre-
130 concentration of GEM on dual gold cartridges followed by thermal desorption in a stream of argon gas and detection by cold vapor atomic fluorescence spectroscopy (CVAFS) at a wavelength of 253.7 nm. Skov et al. (2004) determined a detection limit of 0.1 ng m⁻³ and a reproducibility of 20 %, at a 95% confidence interval (CI) and above 0.5 ng m⁻³. The instrument was manually calibrated with injections of a known amount of mercury before and after the campaigns and auto-calibrated in the field every 25th hour by an internal permeation source.

135 GOM and PHg were collected using a Tekran 1130 and 1135 speciation unit, respectively, upstream of the GEM analyzer, at a flow rate of 10 L min⁻¹. GOM was sampled onto potassium chloride (KCl) coated denuders. After sample collection, the denuders were flushed in a stream of zero air supplied from the 1130 pump module, then heated to 500°C during which GOM was thermally decomposed to GEM and detected by the Tekran 2537A analyzer. Denuders were exchanged weekly. PHg was sampled onto quartz filters, thermally released in a stream of zero air at 800 °C, and pyrolyzed on quartz
140 chips also at 800 °C (for details about denuder and quartz filter performance and coating procedure, see Landis et al. (2002)). The cutoff size for PHg was < 2.5 µm. For the 2019 campaign, the sampling time was 80 minutes, while for the 2020 campaign the sampling time was 60 minutes. Due to technical issues during the 2019 campaign, measurements of PHg were not available. The limit of detection (LOD) for both GOM and PHg was calculated as three times the standard deviation (s.d.) of blanks values for the flush cycles, excluding the first measurement in a flush cycle as the heated sampling line still contains ambient
145 air. The LODs for the 2019 and 2020 campaigns were 0.180 and 0.684 pg m⁻³, respectively. With the KCl denuders being prone to unequal collection efficiencies for different GOM species and artifacts (Gustin et al., 2015) and the internal signal integration routine biasing the concentrations low (Slemr et al., 2016; Ambrose, 2017), the GEM and GOM concentrations are likely a lower limit (Huang and Gustin, 2015; Huang et al., 2017; Maruszczak et al., 2017).

2.3 Ancillary measurements

150 Meteorological parameters including wind speed, wind direction, air temperature, relative humidity, radiation, and snow depth were measured at Villum on a time resolution of 5 minutes. Ground-level H₂O mixing ratios were calculated using ambient temperature, RH, and pressure (Bolton, 1980; Weiss-Penzias et al., 2015). Ozone (O₃) was measured at Villum using a photometric O₃ analyzer (API M400) at 1 Hz, averaged to a 30-minute arithmetic mean. The detection limit was 1 parts per billion by volume (ppbv), with an uncertainty of 3% for measured concentrations above 10 ppbv and 6% below, respectively,
155 on a 95% CI (Nguyen et al., 2016). All measurements used in this study were averaged (median) to correspond temporally to GOM and PHg sampling intervals.

2.4 Particle number size distribution and black carbon

Particle number size distributions (PNSD) from 0.3 to 10 μm were measured using an optical particle sizer (OPS, TSI 3330) on a 10-minute time resolution. This size range is representative of coarse mode particles and a fraction of accumulation mode particles. The entire particle size spectrum was integrated to give the coarse mode particle number concentration (N_{Coarse}). The OPS was located at Villum and the data were vigorously quality controlled for abnormal instrument diagnostic parameters (RH, flow rate, and temperature) and the influence of local pollution (i.e., vehicles and activities from Station Nord).

Black carbon (BC) concentrations were measured using a MAGEE AE33 aethalometer (Drinovec et al., 2015) at a 1-minute time resolution. The instrument is an absorption photometer that continuously collects aerosol particles onto a filter and measures light absorption from the resulting filter spot containing the aerosol particles. The AE33 automatically corrects for filter-loading effects by measuring absorption on a reference filter and operates at seven wavelengths: $\lambda = 370, 470, 520, 590, 660, 880, \text{ and } 950 \text{ nm}$. By using a standard BC mass absorption cross-section (MAC) of $7.77 \text{ m}^2 \text{ g}^{-1}$ at 880 nm, these absorption coefficients are converted to equivalent black carbon (eBC) mass concentrations. It has been found that the aethalometer overestimates BC concentrations at Arctic sites compared to co-located absorption photometers (Backman et al., 2017). To account for this, an Arctic harmonization factor was used, adapted from Backman et al. (2017) to suit the newer aethalometer model. This has been widely used for Arctic datasets (Schmeisser et al., 2018; Zanatta et al., 2018; Schacht et al., 2019). Substantial uncertainties may arise from cross-sensitivity to scattering in the instrument, especially for Arctic aerosols, which are typically highly scattering. This uncertainty is estimated to be around 15% at Villum, using typical values of single scattering albedo (SSA) and previously determined uncertainty studies (Weingartner et al., 2003; Drinovec et al., 2015).

2.5 Air mass history analysis

Air mass history was interrogated by use of the HYSPLIT trajectory model (Draxler and Hess, 1998; Rolph et al., 2017). Air mass back-trajectories of 240-hour length were calculated arriving at 50 m above ground level for every hour during the two campaigns. The trajectory starting height of 50 m was selected as a compromise between capturing air masses that are representative of our sampling site and avoiding trajectories intercepting the surface, which can produce unrepresentative trajectories (Stohl, 1998); trajectories were also initialized at 20 m, which produced similar trajectory paths but often intercepted the surface. For the 2019 campaign, the mixed layer varied from 25 to 554 m, with a median \pm median absolute deviation (m.a.d.) of $74 \pm 131 \text{ m}$, and a bimodal diurnal profile with minima at night and peaks at 5:00 and 15:00 of ~ 80 and $\sim 85 \text{ m}$. For the 2020 campaign, the mixed layer varied from 25 to 204 m, with a median \pm median absolute deviation (m.a.d.) of $34 \pm 21 \text{ m}$, and a bimodal diurnal profile with minima at night and peaks at 13:00 and 18:00 of ~ 40 and $\sim 50 \text{ m}$. The trajectory length of 240 hours was selected to capture the lifetime of GOM in the atmosphere and assess the geographical extent of air masses. Global Data Assimilation System (GDAS) meteorological data on a 1° spatial resolution, employing modeled vertical velocity, were used as input for the model. The HYSPLIT model output included meteorological variables along the trajectory

path including relative humidity, precipitation, mixed layer height, and H₂O mixing ratio. Precipitation along each trajectory
190 was integrated to calculate the amount of accumulated precipitation. These parameters along with active fire data were utilized
to inspect the geo-physical history of air masses arriving at Villum during the campaign periods (Greene et al., 2017; Greene,
2020). Active fire data were provided by NASA's Fire Information for Resource Management System (FIRMS), active fire
data from NASA's Moderate Resolution Imaging Spectroradiometer (MODIS), and NASA's Visible Infrared Imaging
Radiometer Suite (VIIRS) (Schroeder et al., 2014).

195 3 Results

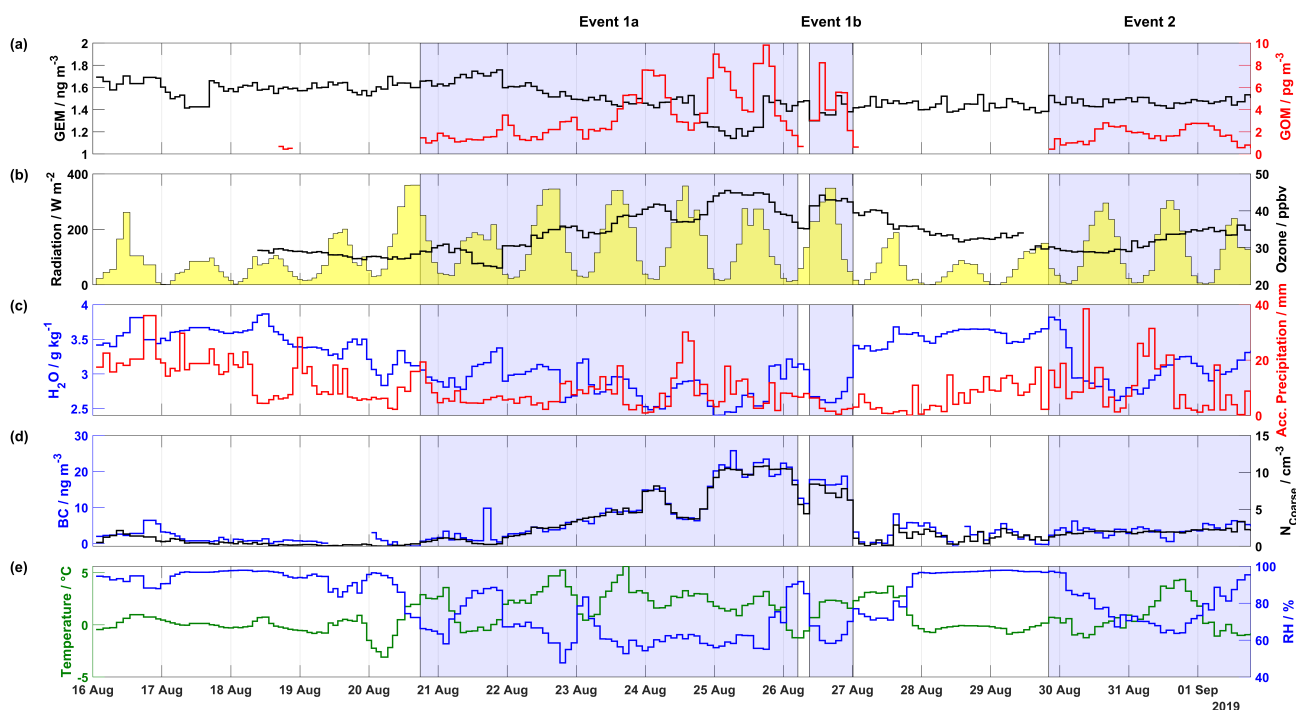
3.1 Atmospheric mercury and ground-level meteorological parameters

From the two campaigns, seven events of enhanced GOM concentrations were observed: three during the 2019 campaign and
four during the 2020 campaign. These events were identified by enhancements of GOM over background levels as well as
meteorological conditions and air mass classification. Results from the 2019 campaign, describing the time series of
200 atmospheric mercury concentrations, ground-level meteorological parameters (radiation, H₂O mixing ratio, temperature, and
RH), accumulated precipitation along the trajectory length, ozone, and aerosol properties (BC concentration and N_{Coarse}) are
presented in Fig. 1. Wind direction, wind speed, and snow depth are displayed in Fig. S1. During the 2019 campaign, there
were three distinct GOM enhancement events: Event 1a from August 20 at 17:45 to August 26 at 05:00, Event 1b from August
26 at 9:00 to August 27 at 00:10, and Event 2 from August 29 at 20:10 to September 1 at 18:20.

205 During the first days of Event 1a (August 21 and 22), GEM increased slightly from ~1.6 to ~1.7 ng m⁻³, then on the
night of August 22, GEM suddenly dropped followed by a slow decrease until the afternoon of August 24 when it precipitously
decreased, reaching a minimum of 1.1 ng m⁻³ on the morning of August 25. GEM then quickly increased back to consistent
levels of ~1.5 ng m⁻³ for the remainder of the measurement campaign including Event 1b and 2. For Event 1, GOM gradually
increased from zero on the afternoon of August 20 to the night of August 24, with the highest value (9.81 pg m⁻³) on August
210 25. On the night of August 25 and into the morning of August 26, GOM quickly decreased from ~8 pg m⁻³ to zero,
corresponding to a concurrent increase in RH and H₂O mixing ratio as well as a concurrent decrease in temperature. As RH
then decreased for Event 1b throughout the day of August 26, GOM once again increased to levels comparable to those
observed on the previous day. A back-trajectory analysis on August 26 revealed that, before arrival at Villum, air masses
traversed the Arctic Ocean, Greenland, then the North Atlantic while experiencing low altitudes 50 hours before arrival (Fig.
215 S2). From August 27 to the evening of August 29, GOM is undetectable, before averaging (median ± m.a.d.) 1.65 ± 0.62 pg
m⁻³ for Event 2.

Concerning the meteorological parameters for Events 1a, 1b, and 2, the wind direction was mainly from the southwest
(Fig. S1), with variable wind speed (3.43 ± 2.02 m s⁻¹, Table S1). The relative humidity was low (< 90 % RH), averaging 67.83
± 8.53 % RH for the 2019 event periods, with Events 1a and 1b experiencing similar levels (~63 ± 5 %, Table S1) and Event
220 2 higher RHs (76.91 ± 7.82 %). During non-event periods, RH was considerably higher (95.70 ± 1.82 %). The temperature was

routinely above freezing, with increased temperature during event periods vs non-event periods, 1.68 ± 1.23 vs -0.09 ± 0.43 °C, respectively. The skies were clear with peak solar radiation above 200 W m^{-2} during event periods. Comparable to RH, H_2O mixing ratios and accumulated precipitation were noticeably higher during non-event periods than event periods with Event 2 experiencing higher values than Events 1a and 1b as well as the lowest levels of GOM (Table S1). On August 23, 24, 25, 26, 27, 28, 29, 30, and 31, GOM experienced a reduction in concentration while accumulated precipitation simultaneously increased. A similar relationship between the H_2O mixing ratios and GOM levels is observed during the first part of Event 1a (August 21 and 22) and the aforementioned pattern during the transition of Event 1a to 1b.



230 **Figure 1.** Overview of mercury, meteorological parameters, ozone, and aerosol properties (BC and N_{Coarse}) measured during
the 2019 campaign including (a) GEM (ng m^{-3}) in black on the left axis and GOM (pg m^{-3}) in red on the right axis, (b) radiation
(W m^{-2}) shaded in yellow on the left axis and ozone (ppbv) in black on the right axis, (c) H_2O mixing ratio (g kg^{-1}) at ground
level in blue on the left axis and accumulated precipitation (mm) in red on the right axis, (d) BC (ng m^{-3}) in blue on the left
axis and N_{Coarse} (cm^{-3}) in black on the right axis, and (e) temperature ($^{\circ}\text{C}$) in green on the left axis and relative humidity (%)
235 in blue on the right axis. The areas shaded in blue indicate Events 1a, 1b, and 2, respectively.

Results from the 2020 campaign, describing the time series of atmospheric mercury concentrations, ground-level meteorological parameters (radiation, H_2O mixing ratio, temperature, and RH), accumulated precipitation along the trajectory length, ozone, and aerosol properties (BC concentration and N_{Coarse}), are presented in Fig. 2. Wind direction, wind speed, and

240 snow depth are displayed in Fig. S3. During the 2020 campaign, four distinct GOM enhancement events are observed: Event 3 from July 22 at 16:35 to July 23 at 13:15, Event 4 from July 24 at 11:55 to July 26 at 13:15, Event 5a from July 30 at 17:00 to August 1 at 13:40, and Event 5a from August 13:40 to August 4 at 09:00. The 2020 campaign experienced higher GEM and GOM concentrations compared to the 2019 campaign. For example, GEM increased from $\sim 1.7 \text{ ng m}^{-3}$ on July 17 to $\sim 2.8 \text{ ng m}^{-3}$ on July 19, only to dip to $\sim 1.7 \text{ ng m}^{-3}$ on July 21 before increasing to $\sim 2.4 \text{ ng m}^{-3}$. These elevated concentrations could be
245 the result of oceanic evasion through open leads and fissures in the consolidated pack ice (Aspmo et al., 2006; DiMento et al., 2019), as air masses experienced extensive surface contact with sea ice on July 19–21 (Fig. S4a–c). Satellite images, which show fractured sea ice surrounding Villum are available at <http://ocean.dmi.dk/arctic/nord.uk.php>. For Event 3, GEM and GOM averaged $1.71 \pm 0.13 \text{ ng m}^{-3}$ and $35.13 \pm 13.98 \text{ pg m}^{-3}$, respectively (Table S1). At the beginning of Event 3, GEM dropped from ~ 2 to $\sim 1.5 \text{ ng m}^{-3}$, while GOM increased from ~ 6 to $\sim 62 \text{ pg m}^{-3}$. For Event 4, GEM and GOM averaged $1.79 \pm$
250 0.09 ng m^{-3} and $8.78 \pm 2.38 \text{ pg m}^{-3}$, respectively (Table S1). During Event 4, GOM peaked at $\sim 14 \text{ pg m}^{-3}$ on July 24 at 13:55 and July 25 at 18:35, while GEM decreased from $\sim 1.9 \text{ ng m}^{-3}$ to $\sim 1.4 \text{ ng m}^{-3}$ before returning to levels of $\sim 1.9 \text{ ng m}^{-3}$ by the end of Event 4, this decrease in GEM during Event 4 is part of an overall decreasing pattern of GEM during the preceding and subsequent days (Fig. 2). For Event 5a, GEM was constant, averaging $1.54 \pm 0.02 \text{ ng m}^{-3}$, with GOM increasing throughout the event while averaging $9.10 \pm 2.43 \text{ pg m}^{-3}$. For Event 5b, GEM displayed a slight decreasing pattern with an average of 1.51
255 $\pm 0.05 \text{ ng m}^{-3}$, GOM decreased from $\sim 14 \text{ pg m}^{-3}$ on August 1 to $\sim 5 \text{ pg m}^{-3}$ on August 2 before increasing until August 4 where GOM began to decrease. For Events 3, 4, and 5, PHg displayed no visible pattern and was constantly near or below LOD.

Meteorological parameters during the 2020 campaign are displayed in Fig. 2 and S3 and summarized in Table S1. Event 3 experienced decreasing temperatures (from ~ 5 to $\sim 1 \text{ }^\circ\text{C}$) and increasing RH (~ 77 to $\sim 92 \text{ } \%$) while Event 4 displayed an opposite pattern of increasing temperatures (~ 5 to ~ 7 , maximum $12 \text{ }^\circ\text{C}$) and similar levels of RH at the beginning ($\sim 77 \text{ } \%$)
260 and end ($\sim 79 \text{ } \%$) of the event with a minimum $\sim 52 \text{ } \%$ in the middle. A similar relationship is observed for H_2O mixing ratios, with low values during Event 3 ($3.83 \pm 0.04 \text{ g kg}^{-1}$) and elevated values for Event 4 ($4.61 \pm 0.23 \text{ g kg}^{-1}$). Accumulated precipitation was slightly higher for Event 3 vs 4, 10.90 ± 4.10 and $8.90 \pm 1.90 \text{ mm}$, respectively, although Event 4 experienced a higher maximum ($\sim 31 \text{ mm}$) on July 25. For Events 3 and 4, the wind direction was mainly from the east with low and stable wind speeds (Fig. S3 and Table S1). Radiation during the start of Event 3 was low ($\sim 125 \text{ W m}^{-2}$) but increased as the event
265 progressed. For Event 5a, the temperature exhibited high values ($10.81 \pm 1.27 \text{ }^\circ\text{C}$) and a diurnal pattern with maxima during the afternoon, low ($< 67 \text{ } \%$) and decreasing RH (minimum $\sim 42 \text{ } \%$), and the wind direction was consistently from the southwest with high wind speeds ($9.30 \pm 1.05 \text{ m s}^{-1}$, max 11.5 m s^{-1} , Fig S3 and Table S1). During the beginning of Event 5a, the H_2O mixing ratio was high ($\sim 5 \text{ g kg}^{-1}$) compared to the end of the event ($\sim 3.5 \text{ g kg}^{-1}$), and accumulated precipitation peaked at the beginning of the event (47.4 mm) and averaged $12.95 \pm 3.4 \text{ mm}$. For Event 5b, the temperature continued to be elevated with
270 a diurnal pattern while RH displayed a decreasing pattern till the end of the event, similar patterns were observed for the H_2O mixing ratios and accumulated precipitation (Fig. 2). During all four events, snow cover was near zero (Fig. S3) and radiation was high with peak values $> 375 \text{ W m}^{-2}$ (except during the beginning of Event 3 and end of Event 4, Fig 2).

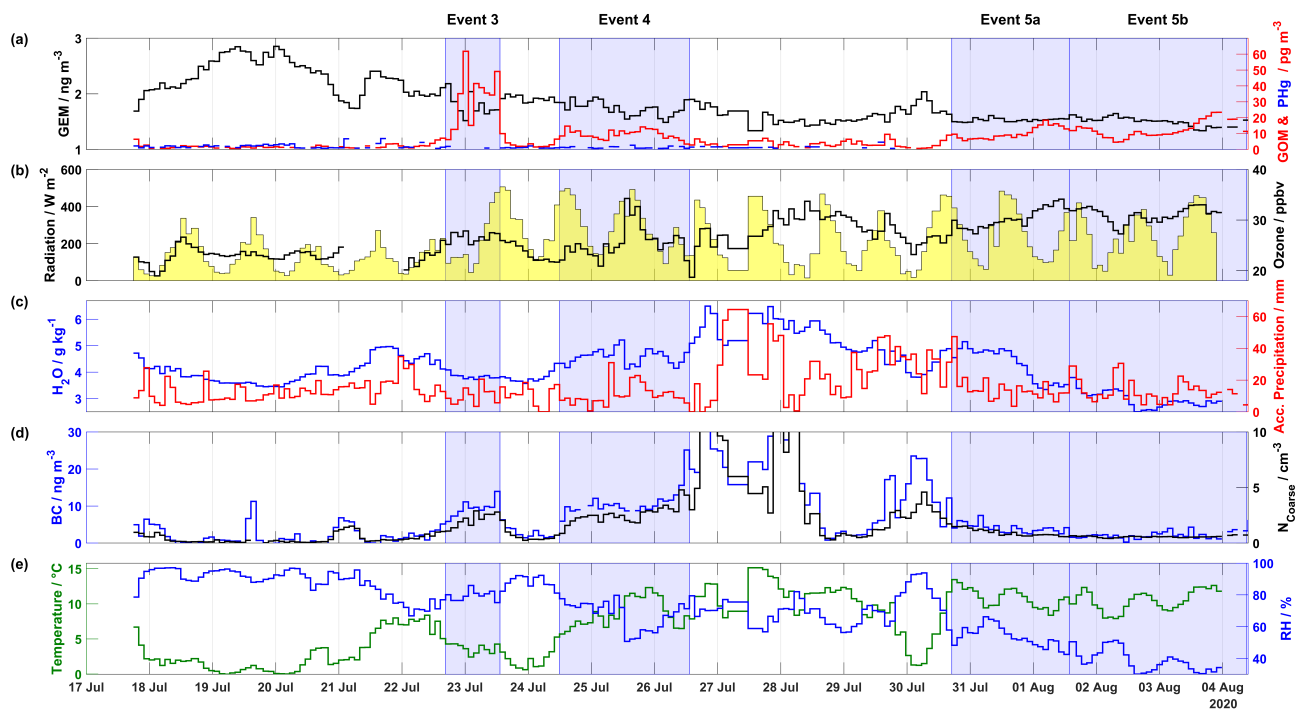


Figure 2. Overview of mercury, meteorological parameters, ozone, and aerosol properties (BC and N_{Coarse}) measured during the 2020 campaign including (a) GEM (ng m^{-3}) in black on the left axis, GOM (pg m^{-3}) in red, and PHg (pg m^{-3}) in blue on the right axis, (b) radiation (W m^{-2}) shaded in yellow on the left axis and ozone (ppbv) in black on the right axis, (c) H_2O mixing ratio (g kg^{-1}) at ground level in blue on the left axis and accumulated precipitation (mm) in red on the right axis, (d) BC (ng m^{-3}) in blue on the left axis and N_{Coarse} (cm^{-3}) in black on the right axis, and (e) temperature ($^{\circ}\text{C}$) in green on the left axis and relative humidity (%) in blue on the right axis. The areas shaded in blue indicate Events 3, 4, 5a, and 5b, respectively. The axis scale for (d) is truncated to show the fine structure of BC and N_{Coarse} during event periods, for the full scale see Fig. 7.

3.2 Air mass history

Contour plots for different meteorological parameters (temperature, relative humidity, radiation, H_2O mixing ratio, and precipitation) and altitude for each hourly trajectory for the 2019 and 2020 campaigns are displayed in Fig. 3 and 4, respectively. Mixed layer height for each step of each hourly trajectory for the 2019 and 2020 campaigns is shown in Fig. S5.

285

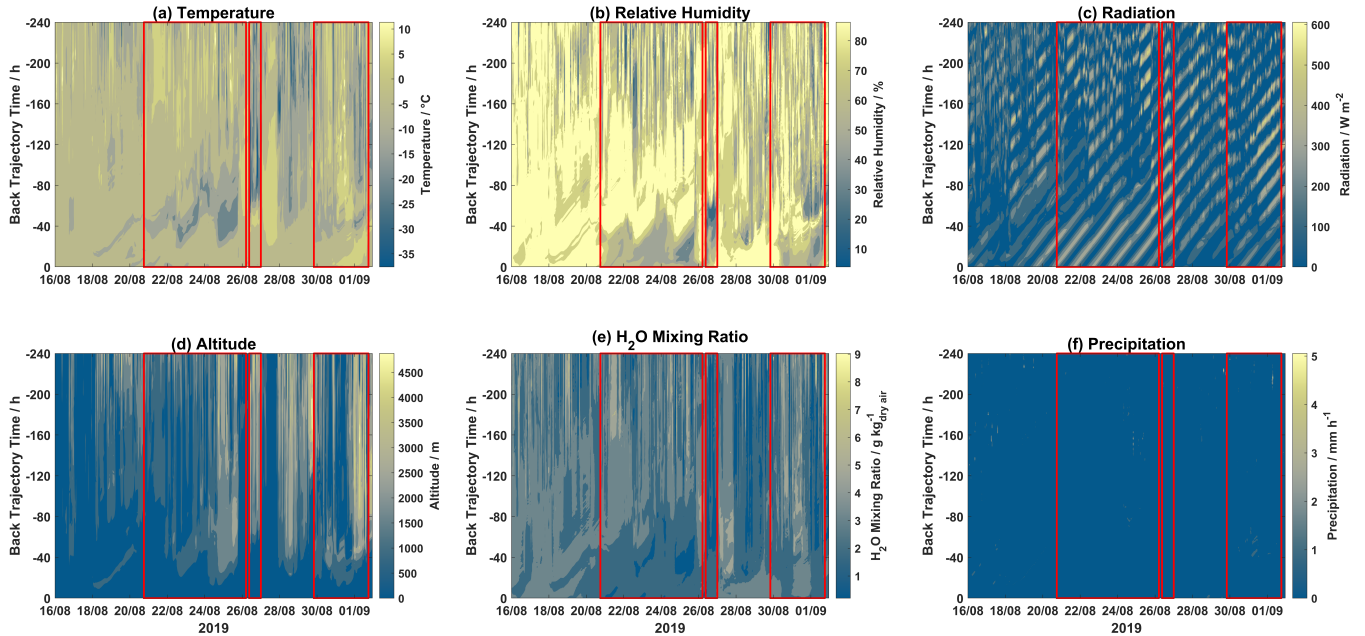
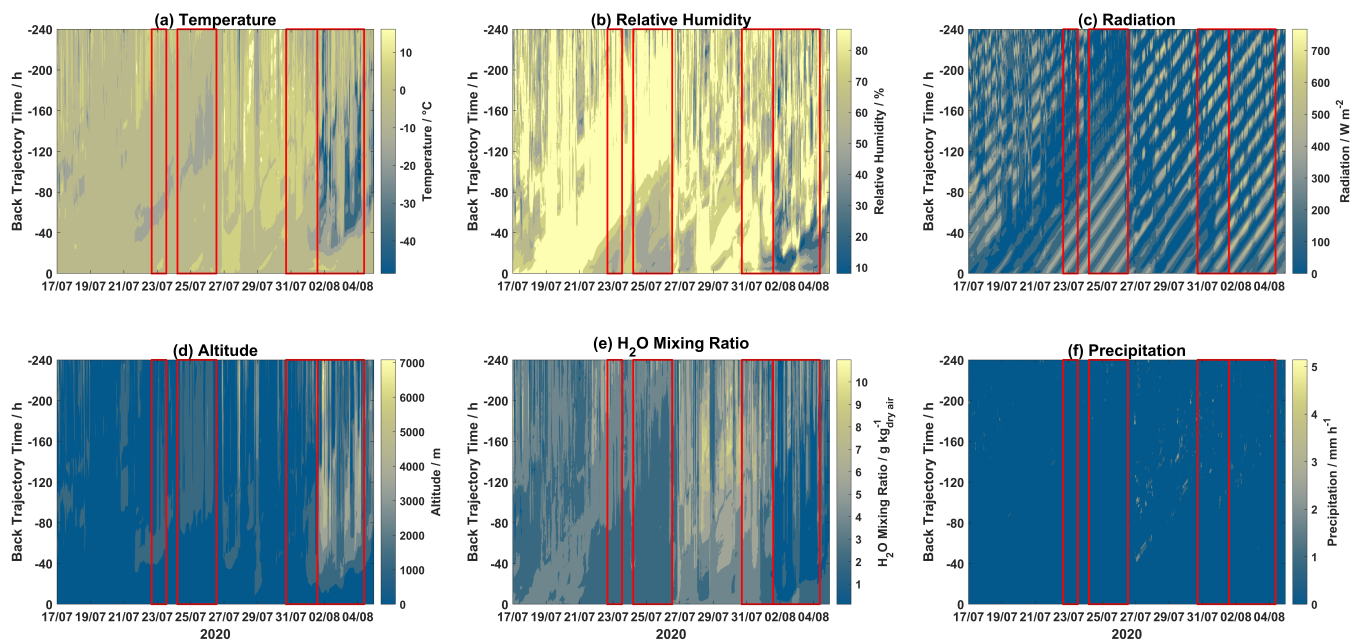


Figure 3. Contour plots of trajectory derived meteorological parameters (a) temperature, (b) relative humidity, (c) solar radiation, (d) altitude, (e) H₂O mixing ratio, and (f) precipitation, along each trajectory for the 2019 campaign. Event periods are outlined in red. The x-axis displays arrival time at Villum, the y-axis displays hours backward in time for each trajectory, and the color bar represents the meteorological parameter.

During Event 1a, after ~120 hours trajectory temperatures were warmer with lower RH values, while H₂O mixing ratios were increased after ~80 hours. Radiation was intense before 80 hours for the entirety of Event 1a, after this time air masses experienced variable radiation, especially on August 21, 22, 24, and 25. Air masses during Event 1a were consistently elevated with the highest altitudes on August 24-26. Precipitation was low except for several episodes which is reflected in the accumulated precipitation (Fig. 1). Event 1b experienced lower temperatures after 80 hours although lower RH before this time, radiation was intense and H₂O mixing ratios were low throughout the trajectory length for the entire event. For the first half of Event 2, air masses were slightly warmer and wetter with lower radiation and decreased altitudes when compared to the second half of this event. During Event 3, temperatures were consistently warm except for a period of colder temperatures around ~60 hours backward. A similar observation is made for RH with high values after ~50 hours although the H₂O mixing ratios were elevated after ~70 hours. Radiation was intense before ~60 hours and low after that time. Event 4 experienced similar conditions to Event 3, although at later times throughout the air mass history. Interestingly, Event 5a and 5b experienced similar levels of GOM (Fig. 2), although Event 5a experienced higher temperatures as well as higher RH and H₂O mixing ratios with trajectories arriving from lower altitudes and being exposed to less radiation. Presuming that an RH greater than 95 % signifies air masses were within a cloud (Schmeissner et al., 2011; Freud et al., 2017), the time spent in-cloud could be

305 calculated for each event. Air masses during Events 1a, 1b, and 2 spent 22.67, 11.67, and 14.28 % of the time in-cloud,
 respectively, and 19.15 % combined. For Events 3, 4, 5a, and 5b, air masses spent 52.58, 38.32, 20.37, and 14.68 % of the
 time in-cloud, and 27.37 % combined. For the 2019 campaign, event air masses spent less time in a cloud compared to non-
 event air masses (29.61 %), both when comparing individual events and combined event periods. For the 2020 campaign, the
 same general pattern is observed when comparing combined event periods, although Events 3 and 4 spent more time in a cloud
 310 compared to non-event air masses (32.59 %, Table S2).



315 **Figure 4.** Contour plots of trajectory derived meteorological parameters **(a)** temperature, **(b)** relative humidity, **(c)** solar radiation, **(d)** altitude, **(e)** H₂O mixing ratio, and **(f)** precipitation, along each trajectory for the 2020 campaign. Event periods are outlined in red. The x-axis displays arrival time at Villum, the y-axis displays hours backward in time for each trajectory, and the color bar represents the meteorological parameter.

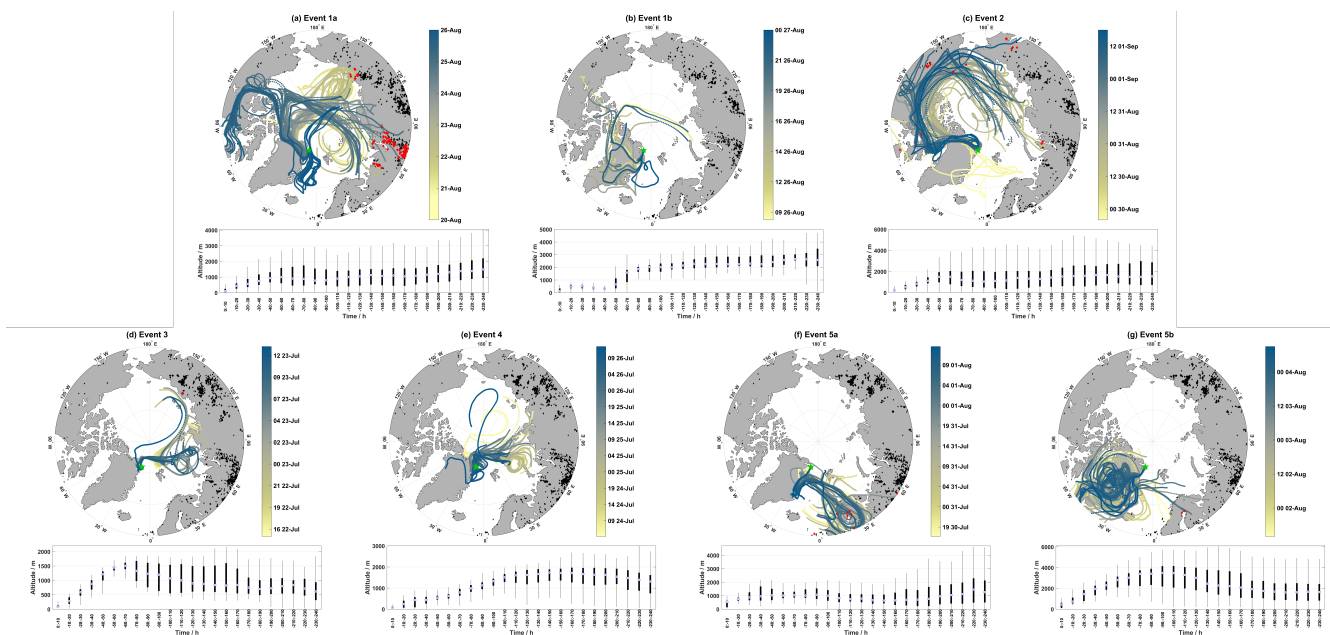


Figure 5. Map of air mass back-trajectories during Events 1–5 in (a) through (g). The top panel shows individual hourly trajectories are colored-coded by the arrival date at Villum as indicated by the color bar (the date format is HH dd-MMM), active fires during each event are in black, active fires intersecting trajectories within 1° latitude/longitude and within 1 hour are in red (active fires from the previous 10 days before the start of an event were included to reflect the trajectory length). The position of Villum is marked by the green star. The bottom panel displays boxplots of the altitude for each event binned in increments of ten hours.

Geospatially, the GOM enhancement events show different source regions. Figure 5a–g shows hourly air mass back-trajectories, combined with active fire data, for each event. To capture the presence of fires in relation to the length of each trajectory, active fires from the previous 10 days before the start of each event and up to the end of each event are marked in black and active fires intersecting trajectories within 2° latitude/longitude and within 2 hours are marked in red. The bottom panels in Figure 5a–g displays the distribution of trajectory altitudes binned in ten-hour increments. Biomass burning (one of the possible causes of active fires) can emit aerosols covering a large size range and varying chemical composition (Reid et al., 2005), therefore active fires were included to analyze their effect on the air mass history during event periods. For Event 1, air masses circulated over the Barents Sea, Kara Sea, and the central Arctic Ocean at the beginning of the event before transitioning to the East Siberian Sea. During the latter part of Event 1a, trajectories experienced continental influence from Eurasia before shifting to the Canadian archipelago, and finally arriving from the Greenland Sea. Trajectories in Event 1a were influenced by active fires during each circulation pattern except for the latter part when air masses passed over the Greenland Sea before arrival, corresponding to reduced GOM concentrations (Fig. 1). Trajectory altitudes during Event 1a were consistently above 1000 m after 120 hours, they experienced a minimum median altitude at 80–90 hours, and descended from

~1000 m approx. 50–60 hours before arrival. The distribution for trajectory altitudes during Event 1a were diverse, with each bin experiencing surface level contact as well as reaching the middle free troposphere (Fig. 5a). For Event 1b, air masses were mainly confined to the Arctic Ocean and central Greenland, with a few trajectories passing over the Canadian archipelago and the Greenland Sea. Median trajectory altitudes spent considerable time above 2000 m after 80 hours, followed by a quick descent to low altitudes for the last 50 hours before arrival at Villum. Event 2 showed a major contribution of air masses from the central Arctic Ocean, North America, and the Canadian archipelago with smaller contributions from the Northern Atlantic just south of Svalbard. There is some influence of active fires from Eurasia, North America, and the Canadian archipelago during this event, although infrequent and at different stages of transport (Fig. 5c). Analogous to Event 1a, median trajectory altitudes during Event 2 were consistently elevated after 120 hours and resided in the surface layer and middle of the free troposphere. Event 2 experienced a minimum median altitude at 80–90 hours and started a descent from ~1500 m approx. 40–50 hours backward. Events 3 showed air masses originating from the Barents Sea and the Arctic Ocean with little influence of active fires. Trajectory altitudes for Event 3 experienced surface layer contact after 200 hours backward, thereafter, started an ascent in the free troposphere from 70–190 hours backward, which was followed by a steep descent from 1500 m at approx. 60–70 before arrival. Event 4 showed a similar spatial extent to Event 3 although with air masses located closer to Villum. Median trajectory altitudes for Event 4 resided at elevated altitudes with surface layer contact only after 200 hours, then started their descent from 1600 m approx. 120 before arrival. For Event 5a, air masses consistently arrived from Northern Scandinavia with extensive influence from active fires. Trajectory altitudes were considerably lower (varying around 1000 m) and experienced surface layer contact after 100 hours, after which they started their descent closer to Villum (20–30 hours backward). For Event 5b, air masses shifted to circulating mainly over the Greenlandic ice sheet, although a few trajectories from the Northern Atlantic and parts of Northern Scandinavia also contributed. Trajectory altitudes showed the highest elevations compared to the other events (Table S2 and Fig. 5g), experienced altitudes around 1600 m after 200 hours, starting around 190 hours backward trajectories ascended from ~2000 m until approx. 90–100 backward where trajectories started to descend from ~3500 m. Other than Events 3 and 4, the geospatial origins of air masses during GOM enhancement events were quite diverse. Events 3 and 4 were only separated by a couple of hours and therefore similar air mass origin is expected for the two events, although interestingly Events 5a and 5b showed quite different air mass origins but were temporally consecutive. Each event displayed a gradual descent from elevated altitudes before reaching Villum, except for Event 1b which experienced a steep descent around 50 hours backward followed by extensive surface layer contact.

365 **3.4 Ozone**

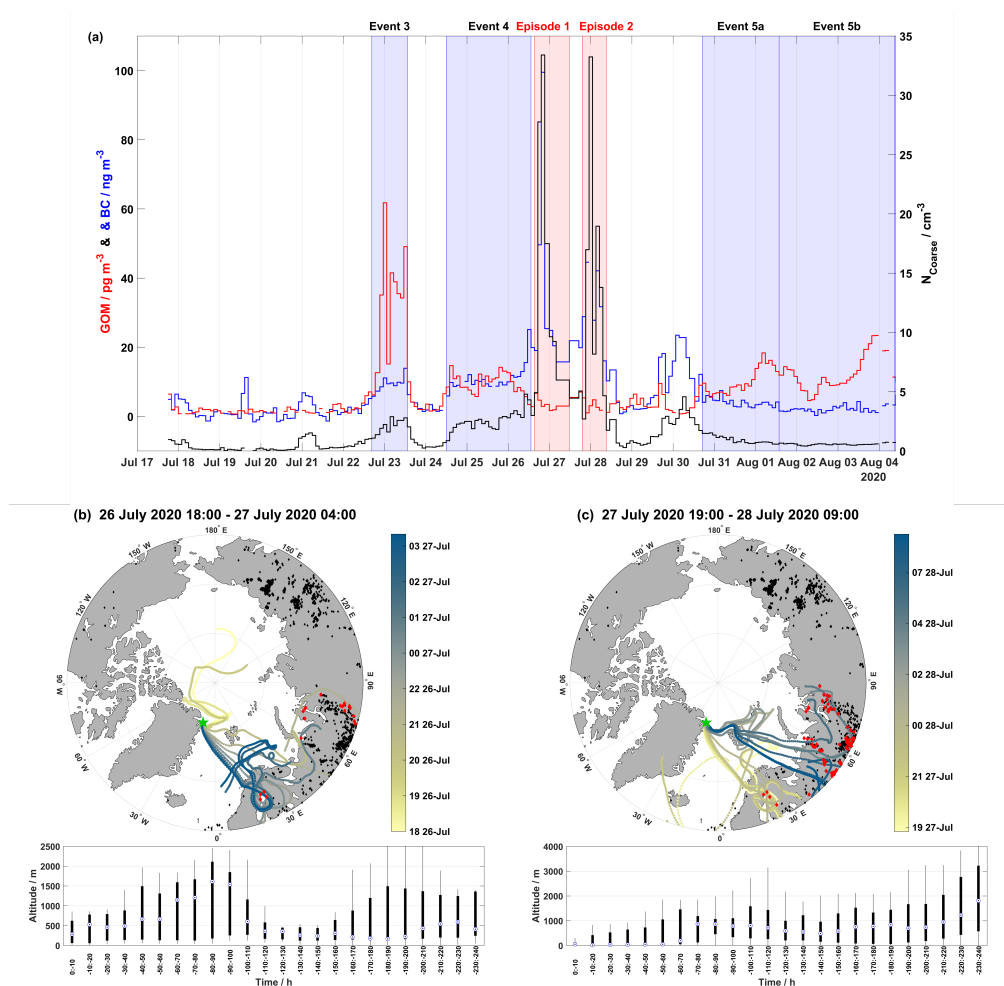
Ozone mixing ratios for the 2019 campaign are displayed in Fig. 1b. Due to technical difficulties, ozone measurements started on August 18 during the 2019 campaign. From August 18 to the beginning of Event 1a, ozone was slightly decreasing with values of ~30 ppbv. For Event 1a, ozone increased concurrently with GOM, both reaching max values of 45.50 ppbv and 9.81 ng m⁻³, respectively, on August 25 (Fig. 1), while GEM exhibits a minimum on August 25 at 1.14 ng m⁻³. The peak ozone level is abnormally high for the late summer (median ± m.a.d. ozone mixing ratio for August 2010–2019 is 24.64 ± 3.14 ppb).

Ozone decreased from this maximum to 35.30 ppbv at the end of Event 1a. For Event 1b, ozone returned to high levels observed at the peak of Event 1a (~40 ppbv). From the end of Event 1a to the beginning of Event 2, ozone steadily decreased. For Event 2, ozone steadily increased from ~29 to ~36 ppbv. For the 2020 campaign, a similar relationship between ozone and GOM is observed (Fig. 2b). Background levels during July (median \pm m.a.d. ozone mixing ratio for July 2010–2019) is 23.92 ± 2.88 ppb. During Event 3, ozone is increasing simultaneously with GOM while GEM is decreasing; for this event, ozone averaged 26.69 ± 0.79 ppb. While this value is not considered elevated for the season, it is elevated over the preceding and subsequent days around Event 3. For Event 4, ozone averaged 25.30 ± 1.63 ppb and is at background levels for much of the event. On July 25, ozone peaked at ~34 ppb before returning to background levels. For Event 5a and 5b, ozone experienced similar levels (Table S1) and followed a similar pattern as GOM, increasing during Event 5a followed by a dip on August 2, then increasing for the remainder of Event 5b.

3.5 Particle number and black carbon

During the non-event periods of the 2019 campaign, the coarse mode particle number concentration (N_{Coarse}) and black carbon (BC) are both low, $0.46 \pm 0.34 \text{ cm}^{-3}$ and $1.22 \pm 1.06 \text{ ng m}^{-3}$, respectively. For Event 1a, N_{Coarse} and BC are both elevated ($3.92 \pm 2.82 \text{ cm}^{-3}$ and $7.30 \pm 4.94 \text{ ng m}^{-3}$, respectively) and increase concurrently with GOM, reaching a maximum concentration of ~11 cm^{-3} and ~26 ng m^{-3} , respectively, on August 25 (Fig. 1d). In-between Event 1a and 1b, N_{Coarse} and BC showed a reduction in concentration, consistent with other parameters during this time (Fig. 1). For Event 1b, N_{Coarse} and BC were elevated and relatively constant, $7.19 \pm 0.95 \text{ cm}^{-3}$ and $16.44 \pm 1.32 \text{ ng m}^{-3}$, respectively. For Event 2, N_{Coarse} and BC returned to low values, although at a higher level compared to non-event periods, $1.99 \pm 0.13 \text{ cm}^{-3}$ and $3.80 \pm 0.59 \text{ ng m}^{-3}$, respectively. This pattern is comparable to the behavior of ozone (Sect. 3.4, Fig. 1b). For the 2020 campaign, a different scenario is observed between N_{Coarse} , BC, and GOM (Fig. 2a and d). For Events 3 and 4, there is a slight enhancement of N_{Coarse} and BC levels when compared to the preceding non-event periods (Fig. 2d). For Event 5a and 5b, both N_{Coarse} and BC are decreasing and low (Fig. 2d and Table S1).

During the 2020 campaign, there are two episodes, the first from July 26 at 17:15 to July 27 at 03:35 and the second from July 27 at 19:05 to July 28 at 09:05, where N_{Coarse} and BC are significantly elevated, reaching up to ~33 cm^{-3} and ~100 ng m^{-3} , respectively, compared to the rest of the campaign (Fig. 7b). These two episodes are observed during non-event periods (Fig. 7b). GOM during these episodes is low, $2.95 \pm 0.78 \text{ pg m}^{-3}$ for the first episode and $2.20 \pm 1.09 \text{ pg m}^{-3}$ for the second episode. These episodes are likely long-range transported, as they are too gradual and long to be identified as local pollution from activities at Station Nord. Another indicator that these episodes were of non-local origin is that ozone remained at constant levels throughout both episodes. If these episodes were of local pollution, then we would expect ozone to decrease as it is titrated by local NO_x emissions. Figures 6a-c show the time series of GOM, N_{Coarse} , and BC on a full-scale axis and air mass back-trajectories for the first and second episodes, combined with active fire data from the previous 10 days to the end of the episode.



405

Figure 6. Time series demonstrating the full scale of N_{Coarse} and BC, along with GOM concentrations shown in (a). The event periods are shaded in blue while the two episodes are shaded in red. Map of air mass back-trajectories during (b) the first episode and (c) the second episode of elevated N_{Coarse} and BC concentrations. The top panels in (b) and (c) show individual hourly trajectories are colored-coded by the arrival date at Villum as indicated by the color bar (the date format is HH dd-
 410 MMM), active fires during each event are in black, active fires intersecting trajectories within 2° latitude/longitude and within 2 hours are in red (active fires from the previous 10 days before the start of an event were included to reflect the trajectory length). The position of Villum is marked by the green star. The bottom panel displays boxplots of the altitude for each event binned in increments of ten hours.

415

4 Discussion

4.1 Factors influencing event vs. non-event periods

For Events 1a, 1b, 2, 4, and 5, the ground-level meteorological parameters mainly associated with GOM enhancement are higher levels of radiation, lower RH, H₂O mixing ratios, and accumulated precipitation when compared to non-event periods (Table S1). For Event 3, radiation was low at the beginning of the event, and temperature and RH displayed an opposite pattern relative to the rest of the events, although H₂O mixing ratios and accumulated precipitation were both low. For the non-event periods in 2019, radiation and temperature were lower while H₂O mixing ratios, accumulated precipitation, and the RH were higher. For the 2020 campaign, non-event periods were more diverse although each displayed a dissimilar pattern in one or more parameters when compared to event periods. For example, at the beginning of the 2020 campaign and during the non-event period between Event 3 and 4, both H₂O mixing ratios and accumulated precipitation were low, however, radiation was also low, while the RH was high (Fig. 2). For the non-event period between Event 4 and 5a, radiation was sufficiently high but H₂O mixing ratios and accumulated precipitation were exceptionally high, while the temperature and RH fluctuated throughout this period (Fig. 2).

The factors influencing event periods at ground level are high levels of radiation, low H₂O mixing ratios, accumulated precipitation, and RH. Higher levels of solar radiation enable the photolysis of reactive halogen species and lower RH and H₂O mixing ratios inhibit the partitioning of GOM into the liquid phase (Laurier, 2003; Soerensen et al., 2010; Brooks et al., 2011; Steen et al., 2011). Interestingly, none of the events were linked to cold temperatures, which has been previously demonstrated to be associated with mercury oxidation through observations in the Arctic (Cole and Steffen, 2010; Ariya et al., 2015; Steffen et al., 2015), theoretical studies (Shepler et al., 2007), and modeling (Toyota et al., 2014). The stability of the Hg-Br intermediate is highly temperature-dependent (Goodsite et al., 2004; Donohoue et al., 2006; Dibble et al., 2012; Goodsite et al., 2012). Lower temperatures aid in the formation of GOM from HgBr, for example, Skov et al. (2004) and Christensen et al. (2004) modeled a surface temperature below -4 °C for mercury depletion to occur in the Arctic, while Brooks et al. (2011) observed a temperature threshold of -15 °C for mercury oxidation to occur at Summit Station, atop the Greenlandic ice sheet. It should be noted that Brooks et al. (2011) detected oxidized mercury at temperatures above this threshold but not above 0 °C. Tarasick and Bottenheim (2002) analyzed ozonesonde records and observed surface temperatures below -20 °C were required for the occurrence of ozone depletion events. Furthermore, Halfacre et al. (2019) and Burd et al. (2017) demonstrated that a frozen heterogeneous surface is required for the propagation of halogen explosion events. The temperature at Villum ranged from -1.2 to 5.6 °C and from 2.4 to 13.5 °C during the 2019 and 2020 event periods, respectively. During AMDEs, ozone and GEM are positively correlated due to mutual reaction with halogen species and are both extremely depleted due to strong halogen explosion events in the boundary layer (Schroeder et al., 1998; Lindberg et al., 2002; Berg et al., 2003; Skov et al., 2004; Brooks et al., 2006; Simpson et al., 2015). However, during event periods ozone was consistently elevated over not only non-event periods but also background levels and displayed positive correlations with GOM during all events (Sect. 3.4, Table S1, and Fig. 7). While ozone mixing ratios were high during GOM enhancement events, they are an order of

magnitude below levels reported in the upper troposphere/lower stratosphere (Talbot et al., 2007), and given the slow rate
450 reaction coefficient (Pal and Ariya, 2004), ozone is an improbable first oxidant of mercury during these campaigns (Calvert
and Lindberg, 2005), although ozone has recently been identified as a second oxidant of Hg^{I} (Saiz-Lopez et al., 2020). While
ozone might be acting as a second oxidant of Hg^{I} , any depletions of ozone during GEM oxidation, either through reaction with
the Hg^{I} intermediate or with halogen species, is likely masked by the elevated levels of ozone in the free troposphere. Therefore,
the high ground-level temperatures, the increased ozone mixing ratios, and the positive correlations observed between ozone
455 and GOM during all events cast doubt on the local in situ production of GOM in the boundary layer.

The differences in air mass history between the event and non-event periods may offer insight into the origin of GOM,
given the doubt associated with in situ oxidation at the surface. In general, air masses during event periods were colder, drier,
arrived from higher altitudes, spent more time above the mixed layer, and less time in a cloud (Table S2). Although, there are
notable exceptions to this pattern: Event 3 experienced high RH values and spent over half of the 240 hours in a cloud, and
460 Event 5a experienced high temperatures and elevated H_2O mixing ratios. Analogous to the ground-level meteorological
parameters, the air mass history during non-event periods was missing one or more of these conditions compared to event
periods. For example, during all non-event periods, air mass arrived from altitudes comparable to event periods although often
experienced decreased radiation and high RH and H_2O mixing ratios, especially closer to Villum. The overall pattern of the
air mass history for event periods appears to be cold, dry air masses arriving from above the mixed layer, higher altitudes, and
465 having spent little time in a cloud. The temperature and altitude parameters are interconnected since with increasing altitude
the temperature will decrease as the air becomes less dense. This suggests the cold, dry, high altitudes of the free troposphere
are facilitating the formation of GOM. Colder temperatures in the free troposphere are likely facilitating the formation of
GOM, by increasing the stability of the Hg^{I} intermediate, while low RHs, H_2O mixing ratios, and less time spent within a cloud
are limiting uptake of GOM into the aqueous phase. Additionally, given the low surface resistance of GOM over snowpack
470 (Skov et al. (2006) estimated a surface resistance of GOM close to zero), the occurrence of dry (and possibly wet) deposition
will increase when air masses come in close contact with the surface layer (i.e., below the mixed layer), resulting in decreased
concentrations.

N_{Coarse} was enhanced during event periods vs non-event periods and for every individual event except for 5b (Table
S2). Coarse mode particles and aerosol optical depth have been shown to be connected to the recycling of bromine during
475 spring in the free troposphere leading to a prolonged lifetime of BrO (Peterson et al., 2017; Bogнар et al., 2020), through the
recycling of halogens on aerosol surfaces. This suggests coarse mode particles could be providing a surface for the propagation
of halogen plumes aloft as demonstrated by Peterson et al. (2017) and Simpson et al. (2017). These observations suggest coarse
mode particles may be providing a heterogenous surface for the propagation of halogen species required for the formation of
GOM and this process is facilitated in the cold, dry, and sunlit environment of the free troposphere.

480 Previous studies have demonstrated the influence of the free troposphere on mercury concentrations within the
boundary layer. In the northern hemisphere, the free troposphere has been established as a source of GOM through modeling
studies (Gratz et al., 2015; Shah and Jaeglé, 2017) and observations from both aircraft campaigns (Talbot et al., 2007; Gratz

et al., 2015) and high altitude sites (Swartzendruber et al., 2006; Faïn et al., 2009; Weiss-Penzias et al., 2015; Fu et al., 2016). Faïn et al. (2009) reported similar observations of the free troposphere acting as a source of oxidized mercury at a high elevation
485 site (3220 m above sea level) in the Rocky Mountains, USA. They also observed that the presence of GOM was dependent on RH. They hypothesized that the build-up of GOM in the free troposphere was governed exclusively by the existence of low RH, possibly due to the lack of scavenging by particles at low RH levels. Modeling studies have also shown the free troposphere to be a source of GOM. Using the GEOS-Chem global chemical transport model, Holmes et al. (2006) and Holmes et al. (2010) identified bromine to be the dominant oxidant of GEM globally, with most of the oxidation occurring in the
490 middle and upper troposphere. Shah and Jaeglé (2017) arrived at a similar conclusion using GEOS-Chem that much of the mercury oxidation by bromine occur in the middle and upper troposphere. Weiss-Penzias et al. (2015) compared the GEOS-Chem model output from two different mercury oxidation schemes (a standard run using bromine and an alternative run using OH-O₃) with observations of mercury speciation (GEM and reactive mercury, which is a combination of GOM and PHg) from five high elevation sites. In both the model output and observations, they observed RM was negatively correlated with GEM
495 and H₂O mixing ratios and positively correlated with ozone. They hypothesized RM was formed in the free tropospheric air from the photo-oxidation of GEM. These studies show the free troposphere to be a source of GOM globally, however, there are a limited number of field studies on GOM in the High Arctic summer and none, to the authors' knowledge, on the influence of the free troposphere on GOM levels. These observations from other locations around the globe add credence to our hypothesis, as they all observed similar conditions during high levels of GOM as we did during event periods. Similar chemical
500 processes are likely the cause of the observations in this study; however, the Arctic atmosphere is largely separated from the mid-latitudes during summer on account of contraction of the polar dome, so there may be some differences in the dynamics, albeit unlikely (Holmes et al., 2010).

4.2 Factors influencing individual events

The general pattern associated with event vs non-event periods showed the cold, dry, sunlit free troposphere the likely origin
505 of the GOM enhancement, although individual events did not always fit this description. Individual events displayed unique features which can offer insight into the specific origins of GOM in the Arctic summer.

Event 1a followed the general pattern for ground-level meteorological parameters and air mass history of dry, warm, and sunlit conditions at ground level (Fig. 1) and cold, dry, sunlit air masses arriving from elevated altitudes (Fig. 3 and 5), along with elevated N_{Coarse} and ozone. GOM during Event 1a was moderately negatively correlated with the H₂O mixing ratio
510 and significant on the 95 % confidence level (CL) using the Spearman Rank correlation (Fig. 7a), although no correlation was found for accumulated precipitation (Fig. 7b). GOM during Event 1a was also strongly positively correlated with ozone, N_{Coarse}, and BC on the 95 % CL (Fig. 7e, g, and i), indicating biomass burning could be a potential factor influencing this event. While active fires might not be directly producing GOM (Friedli et al., 2003), they can explain elevated levels of N_{Coarse}, BC, and ozone (Andreae, 2019). Indeed, trajectories during Event 1a experienced extensive intersection with active fires, especially
515 during the first half of the event, under a range of altitudes during transport (Fig. 5a). This range of altitudes could allow for

injected active fire emissions to be entrained into the event air mass. Coarse mode particles emitted from active fires could provide a heterogeneous surface for halogen recycling. Although there were no intersections with trajectories and active fires during the second half of this event, coarse mode particles could arise from other sources (e.g., sea salt aerosol) or result from interactions occurring beyond the length of the trajectories. Thus, while Event 1a exhibited the general pattern for GOM formation in the cold, dry, and sunlit free troposphere, emissions of coarse mode aerosols from active fires likely influenced this event.

On the morning of August 26, GOM concentrations dropped to zero which marked the end of Event 1a and the beginning of Event 1b. Event 1b experienced similar conditions at ground level, although the air masses were colder, drier, and from higher altitudes with increased radiation (Table S2 and Fig. 3). During Event 1b, GOM displayed a moderately negative correlation with H₂O mixing ratios, although was only significant on the 90 % CL, and was not correlated with accumulated precipitation (Fig. 7a and c). GOM during Event 1b was strongly positively correlated with ozone on the 95 % CL and displayed moderate correlations with N_{Coarse} and BC however they were not statistically significant (Fig. 7e, g, and i). Air masses during this event were confined to the Arctic, exhibited no intersection with active fires, and experienced extensive surface layer contact 50 hours before arrival, yet this event showed similar levels of GOM when compared to Event 1a. Even though air masses experienced surface layer contact 50 hours backward, they were extremely dry and previously resided aloft under cold temperatures (Fig. 3). These conditions are conducive for the formation of GOM and inhibit its removal. The source of coarse mode particles could be emissions from active fires on timescales greater than 240 hours, given the strong correlation with ozone and the moderate yet insignificant correlations with N_{Coarse} and BC (Fig. 7g and i), or possibly other sources such as sea salt. GOM during Event 1b appears to be formed in the cold, dry, sunlit free troposphere, with an unknown source of coarse mode aerosols.

Event 2 displayed the overall pattern of warm, dry, sunlit conditions at ground level accompanied by cold, dry, sunlit conditions in the free troposphere, similar to Event 1a and 1b, although Event 2 exhibited increased accumulated precipitation and H₂O mixing ratios relative to the other events in 2019 (Fig. 1c). GOM during Event 2 showed a weak correlation with H₂O mixing ratios and accumulated precipitation, with only the former being significant on the 95 % CL (Fig. 7a and c). N_{Coarse} and BC showed no enhancement and were constant, while ozone started low and increased throughout the event. GOM during Event 2 was weakly positively correlated with ozone, N_{Coarse}, and BC and none showed a significant correlation at the 95 % CL (Fig. 7e, g, and i). Air masses at the beginning of Event 2 originated from the Greenland Sea then transitioned to a circulation pattern starting near Eurasia before traversing over North America (Fig. 5), and the intersection with active fires was present albeit infrequent. If active fires were influencing GOM concentrations during this event, their signature is likely masked by the increased levels of accumulated precipitation and H₂O mixing ratios, which is also likely responsible for the decreased levels of GOM, N_{Coarse}, and BC during Event 2 relative to 1a and 1b (Table S2), as well as weak correlations. Therefore, the observed levels during Event 2 are likely the result of GOM formation in the cold, dry, sunlit free troposphere and the source of coarse mode particles was possibly active fires, with the decreased levels of GOM, N_{Coarse}, and BC due to wet removal.

550 Event 3 showed the largest observed levels of GOM but showed no obvious features indicating the cause. Radiation, RH, and temperature displayed the opposite pattern for GOM formation, with low levels of radiation, high and increasing values of RH, and decreasing temperatures during the beginning of the event. H₂O mixing ratio and accumulated precipitation both showed low values compared to non-event periods (Fig. 2b), with GOM showing a moderate correlation with H₂O mixing ratios and no correlation with accumulated precipitation (Fig. 7b and c). Ozone showed an enhancement during this event but was low compared to other events, and did not show a correlation with GOM (Fig. 7f). N_{Coarse} and BC both displayed 555 enhancements during this event and were both strongly correlated with GOM (Fig. 7h and j). Air masses originated from the Arctic Ocean and the Barents Sea, with only one active fire intersecting trajectories in western Russia (Fig. 5d). The air mass history of this event exhibited the highest temperatures and RHs, the lowest altitudes, as well as the most time spent above the mixed layer and the most time within a cloud (Table S2). However, this event did experience cold, dry, and sunlit conditions several hours before arrival (Fig. 4), and a steep descent before arrival (Fig 5d). The free troposphere has been shown to be a 560 source of aerosol particles to the boundary layer in the Arctic through entrainment and cloud-mediated transport (Igel et al., 2017). It is possible that the extended time this event spent within a cloud resulted in the cloud mediated transport of free troposphere constituents to the surface layer (Igel et al., 2017), although possible aqueous phase oxidation of Hg⁰ cannot be ruled out (Lin and Pehkonen, 1998; Lyman et al., 2020). Activated and interstitial aerosol particles and GOM could also have 565 undergone evaporation in the warm surface layer temperatures (Fig. 2). This event experienced favorable conditions for GOM formation (cold, dry, and sunlit air masses from aloft) shortly before arrival followed by a quick descent into the surface layer, and these conditions could create a situation where GOM formation is favored and the removal is inhibited, resulting in the high levels. This is however a hypothesis that requires further research.

Event 4 occurred approx. one day after Event 3, experienced a similar geographical origin, similar levels of ozone, 570 accumulated precipitation, N_{Coarse}, and BC, however, the ground level meteorological parameters showed differences in the amount of radiation, H₂O mixing ratios, temperatures, and RHs (Fig. 2 and 5, Table S1). The temperature and RH during Event 4 displayed the general pattern observed for GOM formation although contrasted with the pattern of temperature and RH during Event 3. While the H₂O mixing ratios at ground level were higher during Event 4 compared to Event 3, they showed no correlation with GOM (Fig. 7b). GOM and ozone during Event 4 showed a weak and insignificant correlation (95 % CL) 575 and showed a moderate significant negative correlation with BC and none with N_{Coarse} (Fig. 7f, h, and j). The air mass history showed Event 4 experienced lower temperatures, RHs, H₂O mixing ratios, and time spent within a cloud as well as higher radiation and altitudes but a similar amount of time above the mixed layer compared to Event 3 (Table S2). Event 4 did not show as steep of a descent as Event 3 (Fig. 5d and e). The amount of time spent within a cloud could indicate cloud-mediated transport to the surface layer and the slower rate of descent, coupled with the increased H₂O mixing ratios at ground level, 580 could lead to increased removal of GOM before being observed at Villum. Event 3 and 4 showed similarities that could indicate cloud-mediated transport from the free troposphere to the surface layer, however, there exist dissimilarities that suggest that Event 4 could be the result of entrainment of GOM formed in the cold, dry, sunlit free troposphere. It appears that the increased

H₂O mixing ratios at ground level during Event 4 is the reason for the decreased levels of GOM compared to Event 3. A definitive conclusion for the origin of this event is currently unavailable.

585 Event 5a exhibited high radiation, H₂O mixing ratios, ozone, and temperature along with low accumulated precipitation, RH, N_{Coarse}, and BC at ground level (Fig. 2). GOM during this event was strongly negatively and significantly correlated with H₂O mixing ratios but displayed no correlation with accumulated precipitation on the 95% CL (Fig. 7b and d). This event showed a strong positive correlation between GOM and ozone and moderately negative, albeit significant, correlations with N_{Coarse} and BC (Fig. 7f, h, and j). Air masses for this event arrived consistently from Northern Scandinavia
590 after low-level transport with high temperatures, RHs, and H₂O mixing ratios and being exposed to less radiation (Fig. 4). Air masses circulated in the vicinity of active fires in Northern Scandinavia before being transported to Villum (Fig. 5f). These conditions are opposite to the pattern identified for GOM formation, the cause of the observed GOM levels could therefore be the extensive interactions between trajectories and active fires, although the influence of anthropogenic pollution cannot be ruled out. Air masses were, however, warm, wet, and traveled at low altitudes under little radiation, and therefore it is
595 reasonable to expect this air mass to be depleted in N_{Coarse} and BC as well as GOM, given the high values of hydrological-related parameters. Ozone was elevated and strongly correlated with GOM during Event 5a (Fig. 2 and 7). Ozone could originate from both anthropogenic and natural sources and ozone is only slightly water-soluble leading to less efficient wet removal (Sander, 2015). GOM observed during Event 5a appears to be the result of emissions either from active fires or anthropogenic sources in Northern Scandinavia.

600 Air masses shifted from circulating Northern Scandinavia to the Greenlandic continent on August 1, which coincided with the start of Event 5b. This event is a good example of the observed pattern of GOM formation: warm, dry, sunlit conditions at ground level and cold, dry, sunlit air masses from the free troposphere (Fig 2 and 4). GOM during this event exhibited no correlation with H₂O mixing ratio, accumulated precipitation, or BC while being strongly correlated with ozone and moderately positively correlated with N_{Coarse} (Fig. 7). Enhancements of GOM, which exhibited a positive correlation with ozone, have also
605 been observed during subsidence events in Antarctica as well (Brooks et al., 2008; Pfaffhuber et al., 2012). However, concentrations of N_{Coarse} and BC were extremely low, which is expected of upper tropospheric air masses above the polar dome, which is extremely pristine (Schulz et al., 2019). With the low concentration of N_{Coarse}, there appears not to be a heterogeneous surface for halogen propagation, although this could be due to particles smaller than 0.3 μm facilitating halogen propagation. Another source of reactive halogen species is the photolysis of halocarbons (Yang et al., 2005; Simpson et al.,
610 2015), although Gratz et al. (2015) found this source to be too slow to explain mercury oxidation in the upper troposphere. The origins of GOM during Event 5b appear to be the result of formation in the cold, dry, sunlit free troposphere over the Greenlandic ice sheet from an unknown source of halogens.

 It is interesting to note the vast differences in air mass history for Events 5a and 5b even though both events observed similar levels of GEM, GOM, ozone, and N_{Coarse} (Fig 2). The main differences between these events lie in the H₂O mixing ratios and RH (both at ground level and during transport), the temperature during transport, and the altitude (Table S1 and S2).
615 The median BC concentration for Event 5a was over double that of 5b, although was low compared to other events influenced

620 by active fires i.e., Events 1a and 1b. (Table S1). During Event 5a, air masses were warmer, wetter, and traveled at lower altitudes compared to Event 5b; these conditions could lead to the removal of GOM, N_{Coarse} , and BC through deposition and uptake into the aqueous phase. It is an intriguing observation that air masses that originated from the European continent and were subject to increased hydrological-related parameters during transport (Event 5a) have a similar composition of GOM, ozone, N_{Coarse} , and BC to air masses that originated over Greenland (Event 5b). Currently, an explanation for these observations is unknown and further research is required to fully resolve the interactions of anthropogenic and natural emissions, transport-related processes, and removal mechanisms that are responsible for these observations.

625 There were two episodes of enhanced N_{Coarse} and BC, as presented in Sect. 3.5 and shown in Fig. 6, which appear to be the result of active fire emissions. These two events were interrupted by large amounts of accumulated precipitation on August 27 (Fig. 2). The air mass history during these two episodes shows warm and wet low altitude trajectories with little radiation (Fig. 3); these conditions are inconducive towards GOM formation as indicated by the low levels of GOM, however, they show greatly enhanced concentrations of N_{Coarse} and BC. Figures 6b and c show the geographical extent and intersection of air masses with active fires during the two episodes, respectively. The first few hours of the first episode show trajectories arriving from the central Arctic Ocean, which could arise from emissions in western Russia on longer timescales than 240 hours, however, the reason is unknown at this time. The trajectories for both episodes intersect active fires in Northern Scandinavia and Russia, this region of Russia has been shown to emit large amounts of BC through flaring (Huang et al., 2015; Böttcher et al., 2021). It should be noted that the term active fires represent a thermal anomaly detected by MODIS and VIIRS and cannot be distinguished between vegetation fires and fires due to flaring (Schroeder et al., 2014). The low-level transport, under wet conditions, will likely result in the removal of a fraction of the emissions from these active fires. However, fresh BC emissions are very hydrophobic (Dusek et al., 2006), and might not be removed as efficiently during transport. Event 5a experienced air mass arriving from Northern Scandinavia having circulated over several active fires, although no large increase in BC was observed (Fig. 2 and 5). The large increase in N_{Coarse} and BC during these two episodes is therefore likely due to the flaring activities in Russia while the observed GOM in Event 5a could possibly be due to vegetation fires, although this cannot be confirmed in this study and anthropogenic sources remain a possibility.

630
635
640

645

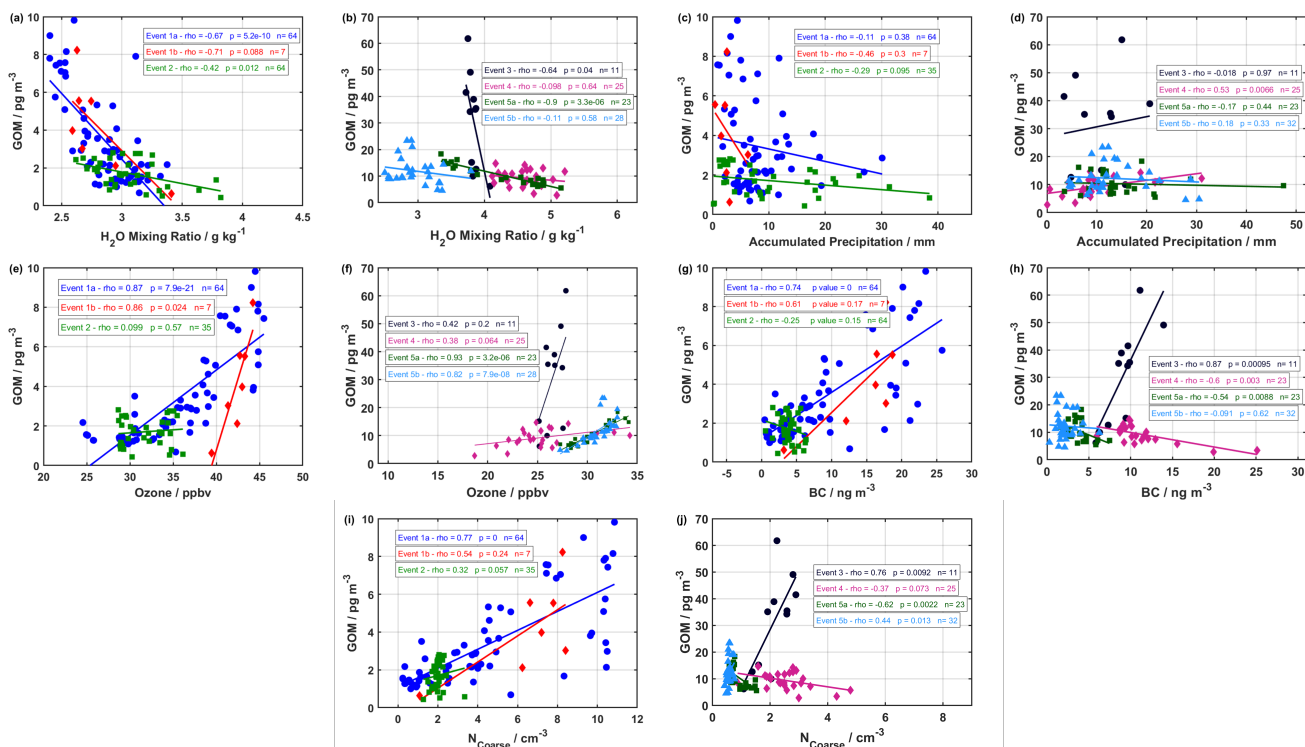


Figure 7. Correlation analysis of GOM with (a) and (b) H₂O mixing ratio, (c) and (d) accumulated precipitation, (e) and (f) ozone, (g) and (h) BC, (i), and (j) N_{Coarse}, for the 2019 and 2020 campaigns, respectively. The Spearman Rank correlation coefficient (ρ), the p-value, and the number of observations are listed for each event in each panel.

5 Conclusion

While the behavior of GEM and GOM during the spring in the High Arctic has received much attention, the dynamics of GOM in the late summer/autumn have seldom been investigated. Therefore, we conducted measurements of GEM, GOM, PHg (only in 2020), meteorological parameters, ozone, and aerosol particle physical properties at Villum Research Station in Northeastern Greenland during the High Arctic summer in 2019 and 2020. The general pattern observed for events of GOM enhancement appears to be cold, dry, sunlit air masses from the free troposphere, as opposed to the low levels of GOM connected with warm and wet air masses with little radiation observed during non-event periods. Coarse mode aerosols provided a heterogeneous surface for halogen propagation during certain events while the source of halogens during other events remains unknown. Analysis of individual events displayed unique origins. GOM observed during Events 1a, 1b, and 2 were likely formed in the cold, dry, sunlit free troposphere with contributions of coarse mode particles from active fires and possibly other sources. Decreased concentrations of GOM during Event 2 were likely due to wet removal. GOM observed during Events 3 and 4 appears to have formed in the cold, dry, sunlit free troposphere from an unknown source of halogens, other processes

are likely contributing, and therefore specific origins of these events cannot be ascertained. The observed GOM during Event 5a was likely the result of emissions from either active fires or anthropogenic activities in Northern Scandinavia. The origins of GOM during Event 5b appear to be the result of formation in the cold, dry, sunlit free troposphere over the Greenlandic ice sheet from an unknown source of halogens. Two episodes of flaring emissions from Russia were observed which did not contribute to enhanced GOM levels.

These measurements and analyses provide insight into the behavior of GOM during summer at a High Arctic station and highlight the complex relationships between GOM formation, removal mechanisms, atmospheric constituents, and meteorological parameters during transport. The behavior of mercury in a changing Arctic climate is still an area with many knowledge gaps, and this work seeks to bridge those gaps, although further research (especially long-term, mercury speciation measurements) is needed.

With changing conditions in the Arctic (i.e., rising temperatures, melting sea ice, longer melt seasons), there is large uncertainty regarding the oxidation and deposition of mercury in response to these changes (Stern et al., 2012). For example, with the Arctic becoming warmer (Jiang et al., 2020) and therefore wetter, the feedback mechanisms on mercury oxidation remain an important scientific question. Warming temperatures will decrease the stability of the Hg^I intermediate as well as increasing atmospheric water vapor, which will favor increased uptake of oxidized mercury into the aqueous phase and its removal by wet deposition. Forest fires are expected to increase in the future (Flannigan et al., 2009; Kelly et al., 2013), which could lead to an increase in coarse mode particles. The magnitude of these effects and their consequences for GOM levels in the High Arctic is still an open question. Given the positive correlation between GOM and coarse mode particles, and their role in halogen activation, changes in the size distribution and chemical composition of aerosol particles could have implications for mercury oxidation. Recent trends in declining sea ice (Stroeve et al., 2012) could increase the sea salt and total aerosol burden, thus potentially increasing mercury oxidation and deposition via increased halogen recycling and particulate mercury deposition. Declining sea ice could also increase GEM evasion from the Arctic Ocean, shifting the Arctic Ocean from a sink to a source (Ariya et al., 2004; Dastoor and Durnford, 2014). Future studies addressing the contribution of the free troposphere to boundary layer GOM concentrations along with flux measurements of dry and wet deposition of GOM in the summer will help answer these questions. The presented work aims to bridge some of the knowledge gaps in mercury processing although further research is needed to advance our understanding of how the behavior of atmospheric mercury will respond in a changing climate. Specifically, we recommend long-term measurements of mercury speciation at more High Arctic stations to obtain more information on seasonality, trends, and the geospatial distribution of atmospheric mercury species.

Financial Support. This study was funded by the Danish Environmental Protection Agency (DANCEA funds for Environmental Support to the Arctic Region project; grant no. 2019-7975) and by the European ERA-PLANET projects of

iGOSP and iCUPE (consortium agreement no. 689443 for both projects). Villum Foundation is gratefully acknowledged for financing Villum Research Station.

Acknowledgments. Thanks to the Royal Danish Air Force, Arctic Command, and the staff at Station Nord for providing logistic support to the project. Christel Christoffersen and Keld Mortensen are gratefully acknowledged for their technical support. We
700 thank NOAA for use of the HYSPLIT model. We acknowledge the use of data from the NASA FIRMS application (<https://firms.modaps.eosdis.nasa.gov/>).

Data availability. All data used in this publication are available to the community and can be accessed by request to the corresponding author Jakob Boyd Pernov (jbp@envs.au.dk).

Author contributions. JBP, BJ, HSK designed the study. JBP and BJ performed the mercury and aerosol sizing measurements.
705 DCT and AM performed the black carbon measurements. JBP performed all data analysis and air mass history analysis. HSK led the project. JBP wrote the manuscript with comments from all co-authors.

Competing interests. The authors declare that they have no conflict of interest.

710

References

- 715 AMAP: AMAP Assessment 2011: Mercury in the Arctic, Arctic Monitoring and Assessment Programme (AMAP), Oslo, Norway, xiv + 193 pp., 2011.
- Ambrose, J. L.: Improved methods for signal processing in measurements of mercury by Tekran® 2537A and 2537B instruments, *Atmos. Meas. Tech.*, 10, 5063-5073, 10.5194/amt-10-5063-2017, 2017.
- 720 Andreae, M. O.: Emission of trace gases and aerosols from biomass burning - an updated assessment, *Atmos Chem Phys*, 19, 8523-8546, 10.5194/acp-19-8523-2019, 2019.
- 725 Angot, H., Dastoor, A., De Simone, F., Gårdfeldt, K., Gencarelli, C. N., Hedgecock, I. M., Langer, S., Magand, O., Mastromonaco, M. N., Nordstrøm, C., Pfaffhuber, K. A., Pirrone, N., Ryjkov, A., Selin, N. E., Skov, H., Song, S., Sprovieri, F., Steffen, A., Toyota, K., Travníkov, O., Yang, X., and Dommergue, A.: Chemical cycling and deposition of atmospheric mercury in polar regions: review of recent measurements and comparison with models, *Atmos Chem Phys*, 16, 10735-10763, 10.5194/acp-16-10735-2016, 2016.
- 730 Ariya, P. A., Dastoor, A. P., Amyot, M., Schroeder, W. H., Barrie, L., Anlauf, K., Raofie, F., Ryzhkov, A., Davignon, D., Lalonde, J., and Steffen, A.: The Arctic: a sink for mercury, *Tellus B: Chemical and Physical Meteorology*, 56, 397-403, 10.3402/tellusb.v56i5.16458, 2004.
- 735 Ariya, P. A., Amyot, M., Dastoor, A., Deeds, D., Feinberg, A., Kos, G., Poulain, A., Ryjkov, A., Semeniuk, K., Subir, M., and Toyota, K.: Mercury physicochemical and biogeochemical transformation in the atmosphere and at atmospheric interfaces: a review and future directions, *Chem Rev*, 115, 3760-3802, 10.1021/cr500667e, 2015.
- 740 Aspö, K., Temme, C., Berg, T., Ferrari, C., Gauchard, P. A., Fain, X., and Wibetoe, G.: Mercury in the atmosphere, snow and melt water ponds in the North Atlantic Ocean during Arctic summer, *Environmental Science & Technology*, 40, 4083-4089, 10.1021/es052117z, 2006.
- 745 Backman, J., Schmeisser, L., Virkkula, A., Ogren, J. A., Asmi, E., Starkweather, S., Sharma, S., Eleftheriadis, K., Uttal, T., Jefferson, A., Bergin, M., Makshtas, A., Tunved, P., and Fiebig, M.: On Aethalometer measurement uncertainties and an instrument correction factor for the Arctic, *Atmos. Meas. Tech.*, 10, 5039-5062, 10.5194/amt-10-5039-2017, 2017.
- 750 Berg, T., Sekkesæter, S., Steinnes, E., Valdal, A.-K., and Wibetoe, G.: Springtime depletion of mercury in the European Arctic as observed at Svalbard, *Science of The Total Environment*, 304, 43-51, [https://doi.org/10.1016/S0048-9697\(02\)00555-7](https://doi.org/10.1016/S0048-9697(02)00555-7), 2003.
- Bognar, K., Zhao, X., Strong, K., Chang, R. Y.-W., Frieß, U., Hayes, P. L., McClure-Begley, A., Morris, S., Tremblay, S., and Vicente-Luis, A.: Measurements of Tropospheric Bromine Monoxide Over Four Halogen Activation Seasons in the Canadian High Arctic, *Journal of Geophysical Research: Atmospheres*, 125, e2020JD033015, 10.1029/2020jd033015, 2020.
- Bolton, D.: The Computation of Equivalent Potential Temperature, *Monthly Weather Review*, 108, 1046-1053, 10.1175/1520-0493(1980)108<1046:Tcocept>2.0.Co;2, 1980.
- 755 Brooks, S., Arimoto, R., Lindberg, S., and Southworth, G.: Antarctic polar plateau snow surface conversion of deposited oxidized mercury to gaseous elemental mercury with fractional long-term burial, *Atmospheric Environment*, 42, 2877-2884, <https://doi.org/10.1016/j.atmosenv.2007.05.029>, 2008.
- 760 Brooks, S., Moore, C., Lew, D., Lefer, B., Huey, G., and Tanner, D.: Temperature and sunlight controls of mercury oxidation and deposition atop the Greenland ice sheet, *Atmos Chem Phys*, 11, 8295-8306, 10.5194/acp-11-8295-2011, 2011.
- Brooks, S. B., Saiz-Lopez, A., Skov, H., Lindberg, S. E., Plane, J. M. C., and Goodsite, M. E.: The mass balance of mercury in the springtime arctic environment, *Geophysical Research Letters*, 33, 10.1029/2005gl025525, 2006.
- 765 Burd, J. A., Peterson, P. K., Nghiem, S. V., Perovich, D. K., and Simpson, W. R.: Snowmelt onset hinders bromine monoxide heterogeneous recycling in the Arctic, *Journal of Geophysical Research: Atmospheres*, 122, 8297-8309, 10.1002/2017jd026906, 2017.

- 770 Böttcher, K., Paunu, V.-V., Kupiainen, K., Zhizhin, M., Matveev, A., Savolahti, M., Klimont, Z., Väätäinen, S., Lamberg, H., and Karvosenoja, N.: Black carbon emissions from flaring in Russia in the period 2012–2017, *Atmospheric Environment*, 254, 118390, <https://doi.org/10.1016/j.atmosenv.2021.118390>, 2021.
- Calvert, J. G., and Lindberg, S. E.: Mechanisms of mercury removal by O₃ and OH in the atmosphere, *Atmospheric Environment*, 39, 3355-3367, <https://doi.org/10.1016/j.atmosenv.2005.01.055>, 2005.
- 775 Christensen, J. H., Brandt, J., Frohn, L. M., and Skov, H.: Modelling of Mercury in the Arctic with the Danish Eulerian Hemispheric Model, *Atmos. Chem. Phys.*, 4, 2251-2257, 10.5194/acp-4-2251-2004, 2004.
- Cole, A. S., and Steffen, A.: Trends in long-term gaseous mercury observations in the Arctic and effects of temperature and other atmospheric conditions, *Atmos. Chem. Phys.*, 10, 4661-4672, 10.5194/acp-10-4661-2010, 2010.
- 780 Dastoor, A. P., Davignon, D., Theys, N., Van Roozendaal, M., Steffen, A., and Ariya, P. A.: Modeling Dynamic Exchange of Gaseous Elemental Mercury at Polar Sunrise, *Environmental Science & Technology*, 42, 5183-5188, 10.1021/es800291w, 2008.
- Dastoor, A. P., and Durnford, D. A.: Arctic Ocean: Is It a Sink or a Source of Atmospheric Mercury?, *Environmental Science & Technology*, 48, 1707-1717, 10.1021/es404473e, 2014.
- 785 Dibble, T. S., Zelic, M. J., and Mao, H.: Thermodynamics of reactions of ClHg and BrHg radicals with atmospherically abundant free radicals, *Atmos. Chem. Phys.*, 12, 10271-10279, 10.5194/acp-12-10271-2012, 2012.
- 790 DiMento, B. P., Mason, R. P., Brooks, S., and Moore, C.: The impact of sea ice on the air-sea exchange of mercury in the Arctic Ocean, *Deep Sea Research Part I: Oceanographic Research Papers*, 144, 28-38, <https://doi.org/10.1016/j.dsr.2018.12.001>, 2019.
- Donohoue, D. L., Bauer, D., Cossairt, B., and Hynes, A. J.: Temperature and Pressure Dependent Rate Coefficients for the Reaction of Hg with Br and the Reaction of Br with Br: A Pulsed Laser Photolysis-Pulsed Laser Induced Fluorescence Study, *The Journal of Physical Chemistry A*, 110, 6623-6632, 10.1021/jp054688j, 2006.
- 795 Douglas, T. A., Sturm, M., Blum, J. D., Polashenski, C., Stuefer, S., Hiemstra, C., Steffen, A., Filhol, S., and Prevost, R.: A Pulse of Mercury and Major Ions in Snowmelt Runoff from a Small Arctic Alaska Watershed, *Environmental Science & Technology*, 51, 11145-11155, 10.1021/acs.est.7b03683, 2017.
- 800 Douglas, T. A., and Blum, J. D.: Mercury Isotopes Reveal Atmospheric Gaseous Mercury Deposition Directly to the Arctic Coastal Snowpack, *Environmental Science & Technology Letters*, 6, 235-242, 10.1021/acs.estlett.9b00131, 2019.
- 805 Draxler, R. R., and Hess, G. D.: An overview of the HYSPLIT_4 modelling system for trajectories, dispersion and deposition, *Australian Meteorological Magazine*, 47, 295-308, 1998.
- Drinovec, L., Močnik, G., Zotter, P., Prévôt, A. S. H., Ruckstuhl, C., Coz, E., Rupakheti, M., Sciare, J., Müller, T., Wiedensohler, A., and Hansen, A. D. A.: The "dual-spot" Aethalometer: an improved measurement of aerosol black carbon with real-time loading compensation, *Atmos. Meas. Tech.*, 8, 1965-1979, 10.5194/amt-8-1965-2015, 2015.
- 810 Durnford, D., and Dastoor, A.: The behavior of mercury in the cryosphere: A review of what we know from observations, *Journal of Geophysical Research*, 116, 10.1029/2010jd014809, 2011.
- 815 Dusek, U., Reischl, G. P., and Hitznerberger, R.: CCN Activation of Pure and Coated Carbon Black Particles, *Environmental Science & Technology*, 40, 1223-1230, 10.1021/es0503478, 2006.
- Faïn, X., Obrist, D., Hallar, A. G., McCubbin, I., and Rahn, T.: High levels of reactive gaseous mercury observed at a high elevation research laboratory in the Rocky Mountains, *Atmos. Chem. Phys.*, 9, 8049-8060, 10.5194/acp-9-8049-2009, 2009.
- 820 Flannigan, M., Stocks, B., Turetsky, M., and Wotton, M.: Impacts of climate change on fire activity and fire management in the circumboreal forest, *Global Change Biology*, 15, 549-560, <https://doi.org/10.1111/j.1365-2486.2008.01660.x>, 2009.

- 825 Freud, E., Krejci, R., Tunved, P., Leaitch, R., Nguyen, Q. T., Massling, A., Skov, H., and Barrie, L.: Pan-Arctic aerosol number size distributions: seasonality and transport patterns, *Atmos Chem Phys*, 17, 8101-8128, 10.5194/acp-17-8101-2017, 2017.
- Friedli, H. R., Radke, L. F., Lu, J. Y., Banic, C. M., Leaitch, W. R., and MacPherson, J. I.: Mercury emissions from burning of biomass from temperate North American forests: laboratory and airborne measurements, *Atmospheric Environment*, 37, 253-267, [https://doi.org/10.1016/S1352-2310\(02\)00819-1](https://doi.org/10.1016/S1352-2310(02)00819-1), 2003.
- 830 Fu, X., Maruscak, N., Heimbürger, L. E., Sauvage, B., Gheusi, F., Prestbo, E. M., and Sonke, J. E.: Atmospheric mercury speciation dynamics at the high-altitude Pic du Midi Observatory, southern France, *Atmos. Chem. Phys.*, 16, 5623-5639, 10.5194/acp-16-5623-2016, 2016.
- 835 Goodsite, M. E., Plane, J. M. C., and Skov, H.: A theoretical study of the oxidation of Hg-0 to HgBr₂ in the troposphere, *Environmental Science & Technology*, 38, 1772-1776, 10.1021/es034680s, 2004.
- Goodsite, M. E., Plane, J. M. C., and Skov, H.: Correction to A Theoretical Study of the Oxidation of Hg₀ to HgBr₂ in the Troposphere, *Environmental Science & Technology*, 46, 5262-5262, 10.1021/es301201c, 2012.
- 840 Gratz, L. E., Ambrose, J. L., Jaffe, D. A., Shah, V., Jaegle, L., Stutz, J., Festa, J., Spolaor, M., Tsai, C., Selin, N. E., Song, S., Zhou, X., Weinheimer, A. J., Knapp, D. J., Montzka, D. D., Flocke, F. M., Campos, T. L., Apel, E., Hornbrook, R., Blake, N. J., Hall, S., Tyndall, G. S., Reeves, M., Stechman, D., and Stell, M.: Oxidation of mercury by bromine in the subtropical Pacific free troposphere, *Geophysical Research Letters*, 42, 10494-10502, 10.1002/2015gl066645, 2015.
- 845 Greene, C. A., Gwyther, D. E., and Blankenship, D. D.: Antarctic Mapping Tools for MATLAB, *Computers & Geosciences*, 104, 151-157, 10.1016/j.cageo.2016.08.003, 2017.
- Greene, C. A.: Arctic Sea ice: <https://www.mathworks.com/matlabcentral/fileexchange/56923-arctic-sea-ice>), access: 2020-01-26, 2020.
- 850 Gustin, M. S., Amos, H. M., Huang, J., Miller, M. B., and Heidecorn, K.: Measuring and modeling mercury in the atmosphere: a critical review, *Atmos. Chem. Phys.*, 15, 5697-5713, 10.5194/acp-15-5697-2015, 2015.
- Gustin, M. S., Dunham-Cheatham, S. M., Huang, J., Lindberg, S., and Lyman, S. N.: Development of an Understanding of Reactive Mercury in Ambient Air: A Review, *Atmosphere*, 12, 73, 2021.
- 855 Halfacre, J. W., Shepson, P. B., and Pratt, K. A.: pH-dependent production of molecular chlorine, bromine, and iodine from frozen saline surfaces, *Atmos. Chem. Phys.*, 19, 4917-4931, 10.5194/acp-19-4917-2019, 2019.
- 860 Holmes, C. D., Jacob, D. J., and Yang, X.: Global lifetime of elemental mercury against oxidation by atomic bromine in the free troposphere, *Geophysical Research Letters*, 33, 10.1029/2006gl027176, 2006.
- Holmes, C. D., Jacob, D. J., Corbitt, E. S., Mao, J., Yang, X., Talbot, R., and Slemr, F.: Global atmospheric model for mercury including oxidation by bromine atoms, *Atmos. Chem. Phys.*, 10, 12037-12057, 10.5194/acp-10-12037-2010, 2010.
- 865 Horowitz, H. M., Jacob, D. J., Zhang, Y., Dibble, T. S., Slemr, F., Amos, H. M., Schmidt, J. A., Corbitt, E. S., Marais, E. A., and Sunderland, E. M.: A new mechanism for atmospheric mercury redox chemistry: implications for the global mercury budget, *Atmos. Chem. Phys.*, 17, 6353-6371, 10.5194/acp-17-6353-2017, 2017.
- 870 Huang, J., and Gustin, M. S.: Uncertainties of Gaseous Oxidized Mercury Measurements Using KCl-Coated Denuders, Cation-Exchange Membranes, and Nylon Membranes: Humidity Influences, *Environmental Science & Technology*, 49, 6102-6108, 10.1021/acs.est.5b00098, 2015.
- Huang, J., Miller, M. B., Edgerton, E., and Sexauer Gustin, M.: Deciphering potential chemical compounds of gaseous oxidized mercury in Florida, USA, *Atmos. Chem. Phys.*, 17, 1689-1698, 10.5194/acp-17-1689-2017, 2017.
- 875 Huang, K., Fu, J. S., Prikhodko, V. Y., Storey, J. M., Romanov, A., Hodson, E. L., Cresko, J., Morozova, I., Ignatieva, Y., and Cabaniss, J.: Russian anthropogenic black carbon: Emission reconstruction and Arctic black carbon simulation, *Journal of Geophysical Research: Atmospheres*, 120, 11,306-311,333, <https://doi.org/10.1002/2015JD023358>, 2015.

- 880 Hynes, A. J., Donohoue, D. L., Goodsite, M. E., and Hedgecock, I. M.: Our current understanding of major chemical and physical processes affecting mercury dynamics in the atmosphere and at the air-water/terrestrial interfaces, in: *Mercury Fate and Transport in the Global Atmosphere: Emissions, Measurements and Models*, edited by: Mason, R., and Pirrone, N., Springer US, Boston, MA, 427-457, 2009.
- 885 Igel, A. L., Ekman, A. M. L., Leck, C., Tjernström, M., Savre, J., and Sedlar, J.: The free troposphere as a potential source of arctic boundary layer aerosol particles, *Geophysical Research Letters*, 44, 7053-7060, [10.1002/2017gl073808](https://doi.org/10.1002/2017gl073808), 2017.
- Jiang, S., Ye, A., and Xiao, C.: The temperature increase in Greenland has accelerated in the past five years, *Global and Planetary Change*, 194, 103297, <https://doi.org/10.1016/j.gloplacha.2020.103297>, 2020.
- 890 Jiao, Y., and Dibble, T. S.: Structures, Vibrational Frequencies, and Bond Energies of the BrHgOX and BrHgXO Species Formed in Atmospheric Mercury Depletion Events, *The Journal of Physical Chemistry A*, 121, 7976-7985, [10.1021/acs.jpca.7b06829](https://doi.org/10.1021/acs.jpca.7b06829), 2017a.
- 895 Jiao, Y., and Dibble, T. S.: First kinetic study of the atmospherically important reactions $\text{BrHg}^{\cdot} + \text{NO}_2$ and $\text{BrHg}^{\cdot} + \text{HOO}$, *Physical Chemistry Chemical Physics*, 19, 1826-1838, [10.1039/C6CP06276H](https://doi.org/10.1039/C6CP06276H), 2017b.
- Jiskra, M., Sonke, J. E., Agnan, Y., Helmig, D., and Obrist, D.: Insights from mercury stable isotopes on terrestrial-atmosphere exchange of Hg(0) in the Arctic tundra, *Biogeosciences*, 16, 4051-4064, [10.5194/bg-16-4051-2019](https://doi.org/10.5194/bg-16-4051-2019), 2019.
- 900 Kamp, J., Skov, H., Jensen, B., and Sorensen, L. L.: Fluxes of gaseous elemental mercury (GEM) in the High Arctic during atmospheric mercury depletion events (AMDEs), *Atmos Chem Phys*, 18, 6923-6938, [10.5194/acp-18-6923-2018](https://doi.org/10.5194/acp-18-6923-2018), 2018.
- Kelly, R., Chipman, M. L., Higuera, P. E., Stefanova, I., Brubaker, L. B., and Hu, F. S.: Recent burning of boreal forests exceeds fire regime limits of the past 10,000 years, *Proceedings of the National Academy of Sciences*, 110, 13055-13060, [10.1073/pnas.1305069110](https://doi.org/10.1073/pnas.1305069110), 2013.
- 905 Landis, M. S., Stevens, R. K., Schaedlich, F., and Prestbo, E. M.: Development and characterization of an annular denuder methodology for the measurement of divalent inorganic reactive gaseous mercury in ambient air, *Environmental Science & Technology*, 36, 3000-3009, [10.1021/es015887t](https://doi.org/10.1021/es015887t), 2002.
- 910 Laurier, F. J. G.: Reactive gaseous mercury formation in the North Pacific Ocean's marine boundary layer: A potential role of halogen chemistry, *Journal of Geophysical Research*, 108, [10.1029/2003jd003625](https://doi.org/10.1029/2003jd003625), 2003.
- 915 Lin, C.-J., and Pehkonen, S. O.: Oxidation of elemental mercury by aqueous chlorine (HOCl/OCl^-): Implications for tropospheric mercury chemistry, *Journal of Geophysical Research: Atmospheres*, 103, 28093-28102, <https://doi.org/10.1029/98JD02304>, 1998.
- Lindberg, S. E., Brooks, S., Lin, C. J., Scott, K. J., Landis, M. S., Stevens, R. K., Goodsite, M., and Richter, A.: Dynamic oxidation of gaseous mercury in the Arctic troposphere at polar sunrise, *Environmental Science & Technology*, 36, 1245-1256, [10.1021/es0111941](https://doi.org/10.1021/es0111941), 2002.
- 920 Lu, J. Y., Schroeder, W. H., Barrie, L. A., Steffen, A., Welch, H. E., Martin, K., Lockhart, L., Hunt, R. V., Boila, G., and Richter, A.: Magnification of atmospheric mercury deposition to polar regions in springtime: The link to tropospheric ozone depletion chemistry, *Geophysical Research Letters*, 28, 3219-3222, [10.1029/2000gl012603](https://doi.org/10.1029/2000gl012603), 2001.
- 925 Lyman, S. N., Cheng, I., Gratz, L. E., Weiss-Penzias, P., and Zhang, L.: An updated review of atmospheric mercury, *Science of The Total Environment*, 707, 135575, <https://doi.org/10.1016/j.scitotenv.2019.135575>, 2020.
- 930 Macdonald, R. W., and Loseto, L. L.: Are Arctic Ocean ecosystems exceptionally vulnerable to global emissions of mercury? A call for emphasised research on methylation and the consequences of climate change, *Environ. Chem.*, 7, 133-138, [10.1071/en09127](https://doi.org/10.1071/en09127), 2010.
- Marusczak, N., Sonke, J. E., Fu, X., and Jiskra, M.: Tropospheric GOM at the Pic du Midi Observatory—Correcting Bias in Denuder Based Observations, *Environmental Science & Technology*, 51, 863-869, [10.1021/acs.est.6b04999](https://doi.org/10.1021/acs.est.6b04999), 2017.

- 935 Muntean, M., Janssens-Maenhout, G., Song, S., Giang, A., Selin, N. E., Zhong, H., Zhao, Y., Olivier, J. G. J., Guizzardi, D., Crippa, M., Schaaf, E., and Dentener, F.: Evaluating EDGARv4.tox2 speciated mercury emissions ex-post scenarios and their impacts on modelled global and regional wet deposition patterns, *Atmospheric Environment*, 184, 56-68, <https://doi.org/10.1016/j.atmosenv.2018.04.017>, 2018.
- 940 Møller, A. K., Barkay, T., Al-Soud, W. A., Sørensen, S. J., Skov, H., and Kroer, N.: Diversity and characterization of mercury-resistant bacteria in snow, freshwater and sea-ice brine from the High Arctic, *FEMS Microbiology Ecology*, 75, 390-401, 10.1111/j.1574-6941.2010.01016.x, 2011.
- 945 Nguyen, Q. T., Glasius, M., Sorensen, L. L., Jensen, B., Skov, H., Birmili, W., Wiedensohler, A., Kristensson, A., Nojgaard, J. K., and Massling, A.: Seasonal variation of atmospheric particle number concentrations, new particle formation and atmospheric oxidation capacity at the high Arctic site Villum Research Station, Station Nord, *Atmos Chem Phys*, 16, 11319-11336, 10.5194/acp-16-11319-2016, 2016.
- 950 Obrist, D., Tas, E., Peleg, M., Matveev, V., Faïn, X., Asaf, D., and Luria, M.: Bromine-induced oxidation of mercury in the mid-latitude atmosphere, *Nature Geoscience*, 4, 22-26, 10.1038/ngeo1018, 2010.
- Pal, B., and Ariya, P. A.: Studies of ozone initiated reactions of gaseous mercury: kinetics, product studies, and atmospheric implications, *Physical Chemistry Chemical Physics*, 6, 572-579, 10.1039/B311150D, 2004.
- 955 Park, J.-D., and Zheng, W.: Human Exposure and Health Effects of Inorganic and Elemental Mercury, *J Prev Med Public Health*, 45, 344-352, 10.3961/jpmph.2012.45.6.344, 2012.
- 960 Peterson, P. K., Pöhler, D., Sihler, H., Zielcke, J., General, S., Frieß, U., Platt, U., Simpson, W. R., Nghiem, S. V., Shepson, P. B., Stirm, B. H., Dhaniyala, S., Wagner, T., Caulton, D. R., Fuentes, J. D., and Pratt, K. A.: Observations of bromine monoxide transport in the Arctic sustained on aerosol particles, *Atmos. Chem. Phys.*, 17, 7567-7579, 10.5194/acp-17-7567-2017, 2017.
- Pfaffhuber, K. A., Berg, T., Hirdman, D., and Stohl, A.: Atmospheric mercury observations from Antarctica: seasonal variation and source and sink region calculations, *Atmos Chem Phys*, 12, 3241-3251, 10.5194/acp-12-3241-2012, 2012.
- 965 Pirrone, N., Cinnirella, S., Feng, X., Finkelman, R. B., Friedli, H. R., Leaner, J., Mason, R., Mukherjee, A. B., Stracher, G. B., Streets, D. G., and Telmer, K.: Global mercury emissions to the atmosphere from anthropogenic and natural sources, *Atmos Chem Phys*, 10, 5951-5964, 10.5194/acp-10-5951-2010, 2010.
- 970 Reid, J. S., Koppmann, R., Eck, T. F., and Eleuterio, D. P.: A review of biomass burning emissions part II: intensive physical properties of biomass burning particles, *Atmos. Chem. Phys.*, 5, 799-825, 10.5194/acp-5-799-2005, 2005.
- Rolph, G., Stein, A., and Stunder, B.: Real-time Environmental Applications and Display sYstem: READY, *Environmental Modelling & Software*, 95, 210-228, 10.1016/j.envsoft.2017.06.025, 2017.
- 975 Saiz-Lopez, A., Travnikov, O., Sonke, J. E., Thackray, C. P., Jacob, D. J., Carmona-García, J., Francés-Monerris, A., Roca-Sanjuán, D., Acuña, A. U., Dávalos, J. Z., Cuevas, C. A., Jiskra, M., Wang, F., Bieser, J., Plane, J. M. C., and Francisco, J. S.: Photochemistry of oxidized Hg(I) and Hg(II) species suggests missing mercury oxidation in the troposphere, *Proceedings of the National Academy of Sciences*, 117, 30949-30956, 10.1073/pnas.1922486117, 2020.
- 980 Sander, R.: Compilation of Henry's law constants (version 4.0) for water as solvent, *Atmos. Chem. Phys.*, 15, 4399-4981, 10.5194/acp-15-4399-2015, 2015.
- 985 Schacht, J., Heinold, B., Quaas, J., Backman, J., Cherian, R., Ehrlich, A., Herber, A., Huang, W. T. K., Kondo, Y., Massling, A., Sinha, P. R., Weinzierl, B., Zanatta, M., and Tegen, I.: The importance of the representation of air pollution emissions for the modeled distribution and radiative effects of black carbon in the Arctic, *Atmos. Chem. Phys.*, 19, 11159-11183, 10.5194/acp-19-11159-2019, 2019.
- 990 Schmeisser, L., Backman, J., Ogren, J. A., Andrews, E., Asmi, E., Starkweather, S., Uttal, T., Fiebig, M., Sharma, S., Eleftheriadis, K., Vratolis, S., Bergin, M., Tunved, P., and Jefferson, A.: Seasonality of aerosol optical properties in the Arctic, *Atmos. Chem. Phys.*, 18, 11599-11622, 10.5194/acp-18-11599-2018, 2018.

- 995 Schmeissner, T., Krejci, R., Ström, J., Birmili, W., Wiedensohler, A., Hochschild, G., Gross, J., Hoffmann, P., and Calderon, S.: Analysis of number size distributions of tropical free tropospheric aerosol particles observed at Pico Espejo (4765 m a.s.l.), Venezuela, *Atmos. Chem. Phys.*, 11, 3319-3332, 10.5194/acp-11-3319-2011, 2011.
- Schroeder, W., Oliva, P., Giglio, L., and Csiszar, I. A.: The New VIIRS 375 m active fire detection data product: Algorithm description and initial assessment, *Remote Sensing of Environment*, 143, 85-96, 10.1016/j.rse.2013.12.008, 2014.
- 1000 Schroeder, W. H., Anlauf, K. G., Barrie, L. A., Lu, J. Y., Steffen, A., Schneeberger, D. R., and Berg, T.: Arctic springtime depletion of mercury, *Nature*, 394, 331-332, 10.1038/28530, 1998.
- Schulz, H., Zanatta, M., Bozem, H., Leaitch, W. R., Herber, A. B., Burkart, J., Willis, M. D., Kunkel, D., Hoor, P. M., Abbatt, J. P. D., and Gerdes, R.: High Arctic aircraft measurements characterising black carbon vertical variability in spring and summer, *Atmos. Chem. Phys.*, 19, 2361-2384, 10.5194/acp-19-2361-2019, 2019.
- 1005 Shah, V., and Jaeglé, L.: Subtropical subsidence and surface deposition of oxidized mercury produced in the free troposphere, *Atmos. Chem. Phys.*, 17, 8999-9017, 10.5194/acp-17-8999-2017, 2017.
- 1010 Shepler, B. C., Balabanov, N. B., and Peterson, K. A.: $\text{Hg}+\text{Br}\rightarrow\text{HgBr}$ recombination and collision-induced dissociation dynamics, *The Journal of Chemical Physics*, 127, 164304, 10.1063/1.2777142, 2007.
- Simpson, W. R., Brown, S. S., Saiz-Lopez, A., Thornton, J. A., and Glasow, R.: Tropospheric halogen chemistry: sources, cycling, and impacts, *Chem Rev*, 115, 4035-4062, 10.1021/cr5006638, 2015.
- 1015 Simpson, W. R., Peterson, P. K., Frieß, U., Sihler, H., Lampel, J., Platt, U., Moore, C., Pratt, K., Shepson, P., Halfacre, J., and Nghiem, S. V.: Horizontal and vertical structure of reactive bromine events probed by bromine monoxide MAX-DOAS, *Atmos. Chem. Phys.*, 17, 9291-9309, 10.5194/acp-17-9291-2017, 2017.
- 1020 Skov, H., Christensen, J. H., Goodsite, M. E., Heidam, N. Z., Jensen, B., Wahlin, P., and Geernaert, G.: Fate of elemental mercury in the arctic during atmospheric mercury depletion episodes and the load of atmospheric mercury to the arctic, *Environmental Science & Technology*, 38, 2373-2382, 10.1021/es030080h, 2004.
- 1025 Skov, H., Brooks, S., Goodsite, M., Lindberg, S., Meyers, T., Landis, M., Larsen, M., Jensen, B., McConville, G., and Christensen, J.: Fluxes of reactive gaseous mercury measured with a newly developed method using relaxed eddy accumulation, *Atmospheric Environment*, 40, 5452-5463, 10.1016/j.atmosenv.2006.04.061, 2006.
- 1030 Skov, H., Hjorth, J., Nordstrøm, C., Jensen, B., Christoffersen, C., Bech Poulsen, M., Baldtzer Liisberg, J., Beddows, D., Dall'Osto, M., and Christensen, J.: The variability in Gaseous Elemental Mercury at Villum Research Station, Station Nord in North Greenland from 1999 to 2017, *Atmos. Chem. Phys. Discuss.*, 2020, 1-22, 10.5194/acp-2019-912, 2020.
- Slemr, F., Weigelt, A., Ebinghaus, R., Kock, H. H., Bödewadt, J., Brenninkmeijer, C. A. M., Rauthe-Schöch, A., Weber, S., Hermann, M., Becker, J., Zahn, A., and Martinsson, B.: Atmospheric mercury measurements onboard the CARIBIC passenger aircraft, *Atmos. Meas. Tech.*, 9, 2291-2302, 10.5194/amt-9-2291-2016, 2016.
- 1035 Soerensen, A. L., Skov, H., Jacob, D. J., Soerensen, B. T., and Johnson, M. S.: Global Concentrations of Gaseous Elemental Mercury and Reactive Gaseous Mercury in the Marine Boundary Layer, *Environmental Science & Technology*, 44, 7425-7430, 10.1021/es903839n, 2010.
- 1040 Sommar, J., Andersson, M. E., and Jacobi, H. W.: Circumpolar measurements of speciated mercury, ozone and carbon monoxide in the boundary layer of the Arctic Ocean, *Atmos Chem Phys*, 10, 5031-5045, 10.5194/acp-10-5031-2010, 2010.
- 1045 Steen, A. O., Berg, T., Dastoor, A. P., Durnford, D. A., Engelsen, O., Hole, L. R., and Pfaffhuber, K. A.: Natural and anthropogenic atmospheric mercury in the European Arctic: a fractionation study, *Atmos Chem Phys*, 11, 6273-6284, 10.5194/acp-11-6273-2011, 2011.

- Steffen, A., Schroeder, W., Bottenheim, J., Narayan, J., and Fuentes, J. D.: Atmospheric mercury concentrations: measurements and profiles near snow and ice surfaces in the Canadian Arctic during Alert 2000, *Atmospheric Environment*, 36, 2653-2661, [https://doi.org/10.1016/S1352-2310\(02\)00112-7](https://doi.org/10.1016/S1352-2310(02)00112-7), 2002.
- 1050 Steffen, A., Bottenheim, J., Cole, A., Ebinghaus, R., Lawson, G., and Leitch, W. R.: Atmospheric mercury speciation and mercury in snow over time at Alert, Canada, *Atmos Chem Phys*, 14, 2219-2231, 10.5194/acp-14-2219-2014, 2014.
- Steffen, A., Lehnherr, I., Cole, A., Ariya, P., Dastoor, A., Durnford, D., Kirk, J., and Pilote, M.: Atmospheric mercury in the Canadian Arctic. Part I: a review of recent field measurements, *Sci Total Environ*, 509-510, 3-15, 10.1016/j.scitotenv.2014.10.109, 2015.
- 1055 Stephens, C. R., Shepson, P. B., Steffen, A., Bottenheim, J. W., Liao, J., Huey, L. G., Apel, E., Weinheimer, A., Hall, S. R., Cantrell, C., Sive, B. C., Knapp, D. J., Montzka, D. D., and Hornbrook, R. S.: The relative importance of chlorine and bromine radicals in the oxidation of atmospheric mercury at Barrow, Alaska, *Journal of Geophysical Research: Atmospheres*, 117, n/a-n/a, 10.1029/2011jd016649, 2012.
- 1060 Stern, G. A., Macdonald, R. W., Outridge, P. M., Wilson, S., Chetelat, J., Cole, A., Hintelmann, H., Loseto, L. L., Steffen, A., Wang, F., and Zdanowicz, C.: How does climate change influence Arctic mercury?, *Sci Total Environ*, 414, 22-42, 10.1016/j.scitotenv.2011.10.039, 2012.
- 1065 Stohl, A.: Computation, accuracy and applications of trajectories - A review and bibliography, *Atmospheric Environment*, 32, 947-966, 10.1016/s1352-2310(97)00457-3, 1998.
- Stroeve, J. C., Serreze, M. C., Holland, M. M., Kay, J. E., Malanik, J., and Barrett, A. P.: The Arctic's rapidly shrinking sea ice cover: a research synthesis, *Climatic Change*, 110, 1005-1027, 10.1007/s10584-011-0101-1, 2012.
- 1070 Swartzendruber, P. C., Jaffe, D. A., Prestbo, E. M., Weiss-Penzias, P., Selin, N. E., Park, R., Jacob, D. J., Strode, S., and Jaeglé, L.: Observations of reactive gaseous mercury in the free troposphere at the Mount Bachelor Observatory, *Journal of Geophysical Research*, 111, 10.1029/2006jd007415, 2006.
- 1075 Talbot, R., Mao, H., Scheuer, E., Dibb, J., and Avery, M.: Total depletion of Hg degrees in the upper troposphere-lower stratosphere, *Geophysical Research Letters*, 34, 5, 10.1029/2007gl031366, 2007.
- Tarasick, D. W., and Bottenheim, J. W.: Surface ozone depletion episodes in the Arctic and Antarctic from historical ozonesonde records, *Atmos. Chem. Phys.*, 2, 197-205, 10.5194/acp-2-197-2002, 2002.
- 1080 Toyota, K., Dastoor, A. P., and Ryzhkov, A.: Air-snowpack exchange of bromine, ozone and mercury in the springtime Arctic simulated by the 1-D model PHANTAS – Part 2: Mercury and its speciation, *Atmos. Chem. Phys.*, 14, 4135-4167, 10.5194/acp-14-4135-2014, 2014.
- 1085 UNEP: UNEP: Minamata Convention on Mercury: <http://www.mercuryconvention.org/Convention/tabid/3426/Default.aspx> access: 2020-11-12, 2013.
- von Glasow, R.: Atmospheric chemistry in volcanic plumes, *Proceedings of the National Academy of Sciences*, 107, 6594-6599, 10.1073/pnas.0913164107, 2010.
- 1090 Wang, S., McNamara, S. M., Moore, C. W., Obrist, D., Steffen, A., Shepson, P. B., Staebler, R. M., Raso, A. R. W., and Pratt, K. A.: Direct detection of atmospheric atomic bromine leading to mercury and ozone depletion, *Proc Natl Acad Sci U S A*, 116, 14479-14484, 10.1073/pnas.1900613116, 2019.
- 1095 Weingartner, E., Saathoff, H., Schnaiter, M., Streit, N., Bitnar, B., and Baltensperger, U.: Absorption of light by soot particles: determination of the absorption coefficient by means of aethalometers, *Journal of Aerosol Science*, 34, 1445-1463, [https://doi.org/10.1016/S0021-8502\(03\)00359-8](https://doi.org/10.1016/S0021-8502(03)00359-8), 2003.
- 1100 Weiss-Penzias, P., Amos, H. M., Selin, N. E., Gustin, M. S., Jaffe, D. A., Obrist, D., Sheu, G. R., and Giang, A.: Use of a global model to understand speciated atmospheric mercury observations at five high-elevation sites, *Atmos. Chem. Phys.*, 15, 1161-1173, 10.5194/acp-15-1161-2015, 2015.

- 1105 Yang, X., Cox, R. A., Warwick, N. J., Pyle, J. A., Carver, G. D., O'Connor, F. M., and Savage, N. H.: Tropospheric bromine chemistry and its impacts on ozone: A model study, *Journal of Geophysical Research: Atmospheres*, 110, 10.1029/2005jd006244, 2005.
- Ye, Z., Mao, H., Lin, C. J., and Kim, S. Y.: Investigation of processes controlling summertime gaseous elemental mercury oxidation at midlatitudinal marine, coastal, and inland sites, *Atmos. Chem. Phys.*, 16, 8461-8478, 10.5194/acp-16-8461-2016, 2016.
- 1110 Zanatta, M., Laj, P., Gysel, M., Baltensperger, U., Vratolis, S., Eleftheriadis, K., Kondo, Y., Dubuisson, P., Winiarek, V., Kazadzis, S., Tunved, P., and Jacobi, H. W.: Effects of mixing state on optical and radiative properties of black carbon in the European Arctic, *Atmos. Chem. Phys.*, 18, 14037-14057, 10.5194/acp-18-14037-2018, 2018.